DCPT-14/03

Prepared for submission to JCAP

arXiv:1402.4737v1 [astro-ph.CO] 19 Feb 2014

Astrophysical black holes in screened modified gravity

Anne-Christine Davis[a] **Ruth Gregory**[b,c] **Rahul Jha**[a] **Jessica Muir**[a,1]

[a]Department of Applied Mathematics and Theoretical Physics, Centre for Mathematical Sciences, University of Cambridge, Wilberforce Road, Cambridge, CB3 0WA, U.K.

[b]Centre for Particle Theory, South Road, Durham, DH1 3LE, UK

[c]Perimeter Institute, 31 Caroline Street North, Waterloo, ON, N2L 2Y5, Canada

E-mail: acd@damtp.cam.ac.uk, r.a.w.gregory@durham.ac.uk, r.jha@damtp.cam.ac.uk, jlmuir@umich.edu

Abstract. Chameleon, environmentally dependent dilaton, and symmetron gravity are three models of modified gravity in which the effects of the additional scalar degree of freedom are screened in dense environments. They have been extensively studied in laboratory, cosmological, and astrophysical contexts. In this paper, we present a preliminary investigation into whether additional constraints can be provided by studying these scalar fields around black holes. By looking at the properties of a static, spherically symmetric black hole, we find that the presence of a non-uniform matter distribution induces a non-constant scalar profile in chameleon and dilaton, but not necessarily symmetron gravity. An order of magnitude estimate shows that the effects of these profiles on in-falling test particles will be sub-leading compared to gravitational waves and hence observationally challenging to detect.

Keywords: Black holes, scalar fields, no hair theorems

[1]Now at University of Michigan

Contents

1 Introduction **1**

2 Screened modified gravity **3**
2.1 Chameleons 4
2.2 Environmentally dependent dilatons 6
2.3 Symmetrons 7

3 Scalar profile of a black hole surrounded by matter **9**
3.1 Chameleon profile 11
3.2 Dilaton profile 16
3.3 Symmetron profile 18

4 Observational implications **20**

5 Conclusions **24**

1 Introduction

Since it was first published nearly a century ago, general relativity (GR) has earned its place as an incredibly successful and well verified theory of gravity (see e.g. [1]). There are however, both theoretical and observational reasons to consider alternatives to, and extensions of, GR. On the one hand, string theory provides a framework for describing quantum gravity, but suggests that we live in more than 4 dimensions. The consequences of these extra dimensions have not been definitively predicted, however, a generic feature of dimensional reduction is that extra fields appear in the low energy gravitational sector. On the other hand, observations of high redshift supernovae indicate that the universe is expanding at an accelerating rate [2, 3], and together with microwave background [4, 5] and large scale structure [6] measurements, suggest that around 70% of the energy density of the universe comes in the form of a 'dark energy' – an energy momentum density which has a large negative pressure and is well modelled by a cosmological constant. Since the magnitude of the cosmological constant is extremely small by particle physics standards, explaining its stability under quantum corrections is a challenge. Finding either a natural explanation for its measured value or an alternative to the constant, is a major motivation for developing and studying modified theories of gravity (see [7] for a review of various approaches). Additionally, studying modified gravity theories allows us to better explore where GR has been tested rigorously and to constrain the low energy properties of quantum gravity theories.

Scalar-tensor theories, which modify gravity by introducing new, non-minimally coupled scalar fields are an extensively studied alternative to GR. They are theoretically attractive because such light scalar fields are generically predicted in the low energy limit of string theory. For a scalar field to affect cosmological expansion, its mass must be of the order of the Hubble scale, $H_0 \sim 10^{-33}\,\mathrm{eV}$. If it interacts with matter however, the presence of a light scalar field will result in a long-range fifth force and would thus be subject to tight constraints from laboratory and solar system tests of gravity, [1, 8, 9]. These constraints are weakened for theories in which the scalar field modifying gravity somehow decouples from matter, or

is "screened," in dense environments. Models with this property are appealing because they can modify the behaviour of gravity on large scales while recovering the behaviour of GR in environments where local tests have been performed. This paper will focus on three particular scalar-tensor theories which have been found to exhibit screening, known as chameleon, [10], environmentally dependent dilaton, [11], and symmetron, [12], modified gravity.

These models have been studied and constrained using laboratory [13–16], solar system [8], cosmological [17], and astrophysical [18] tests. These investigations all have one thing in common: they probe gravity in a regime where gravitational fields and space-time curvatures are relatively weak. In the near future, the direct detection of gravitational waves from compact binary systems will allow us to constrain the behaviour of gravity in the strong field, large curvature regime. Accordingly, attention has increasingly focussed on efforts to test gravity by studying the dynamics of compact objects such as neutron stars and black holes, [19, 20]. It is thus natural to ask whether observations of black holes might provide new constraints on screened modified gravity.

Inevitably, when studying black holes in the context of a modified gravity theory one has to re-examine the uniqueness of exact solutions, that is, whether the extra physical fields add extra degrees of freedom to the black hole solutions, usually referred to as "black hole hair", [21]. Recently, these "no hair" theorems, originally proven to demonstrate black holes could not carry extra charges measurable at infinity, have been taken in a far stronger context to mean black holes cannot have nontrivial scalar (or other profiles). In fact, this looser definition of 'hair', referred to as *dressing* in [22], has been known to be quite possible for many years, starting with the (unstable) coloured black holes of [23], or the (stable) black monopoles, [24], quantum hair, [25, 26], as well as the explicit vortex hair of [22].

In scalar tensor gravity, a number of no-hair theorems (i.e., demonstrating that the scalar fields takes a constant value around an isolated black hole) have been proven, [27–29] (although note the assumptions behind these theorems may not always correspond to desired physical situations, [30]). The results of these theorems have been extended to binary black hole systems using perturbative, [31, 32], and numerical, [33], calculations, demonstrating that dynamical spacetimes with two interacting black holes in scalar-tensor theory will be indistinguishable from general relativity. This might seem to imply that black hole systems will not be useful for constraining screened modified gravity, however, these theorems do not take into account cosmological backgrounds, in which the scalar field will typically be dynamical. A study of cosmologically evolving black holes with a canonical scalar field, [34], shows that the scalar field does evolve on the event horizon of the black hole, though there is no evidence for an additional scalar charge. Indeed, there are several solutions in the literature which allow for nontrivial scalar fields around black holes, [35–37, 42], although to be fair, many are singular, or "engineered".

We will show that the simple arguments used to determine the lack of hair or dressing can break down in the case of screened modified gravity even for static solutions, where the properties of the scalar are strongly dependent on the local matter density, and can allow for nontrivial scalar fields around conventional (i.e. non-singular) Schwarzschild black holes. This paper focuses on removing the requirement that the black hole exist in a vacuum. This consideration is clearly relevant for astrophysical black holes that are typically observed in galaxies or galactic centres, and can have energetic accretion discs. In order to explore this question, we consider spherically symmetric distributions of matter around a black hole in screened modified gravity. We perform a 'probe' calculation, in that we explore the scalar profile around the black hole without considering the corresponding modification of the black

hole geometry. We are therefore not looking at issues of time dependent black holes, such as discussed in [38–41, 43], as we will see nontrivial profiles even in the static case.

Strictly speaking, a non-uniform matter distribution will result in a non-uniform scalar field profile due to the non-minimal coupling of the scalar to gravity. We expect that the complete picture will be a superposition of multipoles, with the dominant features being encapsulated by the monopole, or spherically symmetric, behaviour. Indeed, if we were to discover that the spherically symmetric case precluded the possibility of black hole hair, then it would be indicative that black holes would not carry hair. Conversely, the discovery of non-trivial spherically symmetric scalar profiles would demonstrate that black holes can indeed carry screened scalar hair, although the full solution would be more complicated and involved than the simple picture presented here.

The layout of the paper is as follows: we introduce screened modified gravity in §2. We then solve for the scalar field profile in §3 under the assumption of spherical symmetry and discuss its effect on the black hole's properties in §4.

2 Screened modified gravity

The basic idea of a screening mechanism is that either the mass of the additional scalar is dependent on the local energy density, or its coupling to matter (or both). Thus, the field can be heavy or decoupled in a dense environment such as our solar system or galaxy, thereby giving no fifth force modifications to gravity, whereas on large cosmological scales at very low densities, the field is much lighter or can couple to matter and therefore give rise to modifications of the gravitational interaction.

We will explore three different models of screened modified gravity: the chameleon mechanism, [10], which occurs when the mass of the scalar field, $m(\phi_0)$, is large enough to suppress the range of the scalar force; the environmental dilaton, [11], where the coupling function between the scalar and matter fields and the mass alter in dense regions; and the symmetron, [12], where the coupling function switches off in dense environments. These mechanisms can be modelled generically with the Einstein frame action

$$S = \int d^4x\sqrt{-g}\left[\frac{M_p^2}{2}R - \frac{1}{2}g^{\mu\nu}\partial_\mu\phi\partial_\nu\phi - V(\phi)\right] + S_m\left[\Psi_i, A^2(\phi)g_{\mu\nu}\right]. \tag{2.1}$$

Here $M_p^2 = 1/8\pi G$ is the Planck mass and S_m is the action for matter fields (denoted generically as Ψ_i), which couple minimally to the Jordan frame metric, $\tilde{g}_{\mu\nu} = A^2(\phi)g_{\mu\nu}$. The details of a particular scalar-tensor theory are completely specified by the scalar potential $V(\phi)$ and the non-linear coupling function $A(\phi)$. We assume $A(\phi)$ is close to 1, writing

$$A(\phi) = e^{\phi\beta(\phi)/M_p} \approx 1 + \phi\frac{\beta(\phi)}{M_p} \tag{2.2}$$

As we are always in the low energy regime, we take $\phi \ll M_p$.

The modified 'Einstein' equation is then written as

$$G^{\mu\nu} = \frac{1}{M_p^2}\left(T_m^{\mu\nu} + T_\phi^{\mu\nu}\right) \tag{2.3}$$

where

$$T_m^{\mu\nu} = 2\frac{\delta S_m}{\delta g_{\mu\nu}},$$
$$T_\phi^{\mu\nu} = \nabla^\mu\phi\nabla^\nu\phi - g^{\mu\nu}\left(\frac{1}{2}g^{\alpha\beta}\nabla_\alpha\phi\nabla_\beta\phi + V(\phi)\right). \tag{2.4}$$

Using $T_m \equiv g_{\mu\nu}T_m^{\mu\nu}$, the scalar field equation is

$$\Box\phi \equiv g^{\alpha\beta}\nabla_\alpha\nabla_\beta\phi = \frac{\partial V}{\partial\phi} - \frac{\partial \ln A}{\partial\phi}T_m. \tag{2.5}$$

Note that in the Einstein frame, the matter stress-energy tensor is not covariantly conserved, rather, we have

$$\nabla_\mu T_m^{\mu\nu} = -\nabla_\mu T_\phi^{\mu\nu} = T_m\frac{\partial \ln A}{\partial\phi}g^{\mu\nu}\partial_\mu\phi. \tag{2.6}$$

This can be interpreted as a 'fifth force' on matter due to its interaction with the scalar field. For a non-relativistic particle, this takes the form

$$\ddot{\mathbf{x}} = -\frac{\partial \ln A}{\partial\phi}\nabla\phi\,. \tag{2.7}$$

It is convenient to define $\rho \equiv -A^{-1}T_m$, which is a conserved density for non-relativistic distributions of matter, [45], in the Einstein frame. Using this formalism, the scalar equation of motion is

$$\Box\phi = \frac{\partial}{\partial\phi}\left[V(\phi) + (A(\phi)-1)\rho\right] \equiv \frac{\partial V_{\rm eff}(\phi,\rho)}{\partial\phi}. \tag{2.8}$$

The fact that dynamics of ϕ are governed by a density-dependent effective potential $V_{\rm eff}(\phi,\rho)$ is the source of the screening behaviour for chameleons, environmentally dependent dilatons, and symmetrons.

2.1 Chameleons

Chameleon models contain a scalar field whose mass is an increasing function of density, which causes the range of any fifth force to be suppressed in dense regions [10]. This means chameleon scalars are screened in dense environments like the solar system, and can evade local observational constraints while still having significant effects on cosmological scales. In these models, it is typically assumed that $\beta(\phi)$ is nearly independent of ϕ throughout the relevant field range, and so can be treated as a constant parameter. The coupling function is therefore taken to be

$$A(\phi) = e^{\beta\phi/M_p}\,. \tag{2.9}$$

A typical chameleon potential is

$$V(\phi) = M^{4+n}\phi^{-n} = V_0\phi^{-n}, \tag{2.10}$$

where $n \geq 1$ is an integer of order one, and we define $V_0 \equiv M^{4+n}$ to simplify notation. Keeping only the leading order term from the coupling function, we see that the effective potential is

$$V_{\rm eff}(\phi,\rho) \approx \frac{V_0}{\phi^n} + \frac{\rho\beta\phi}{M_p}, \tag{2.11}$$

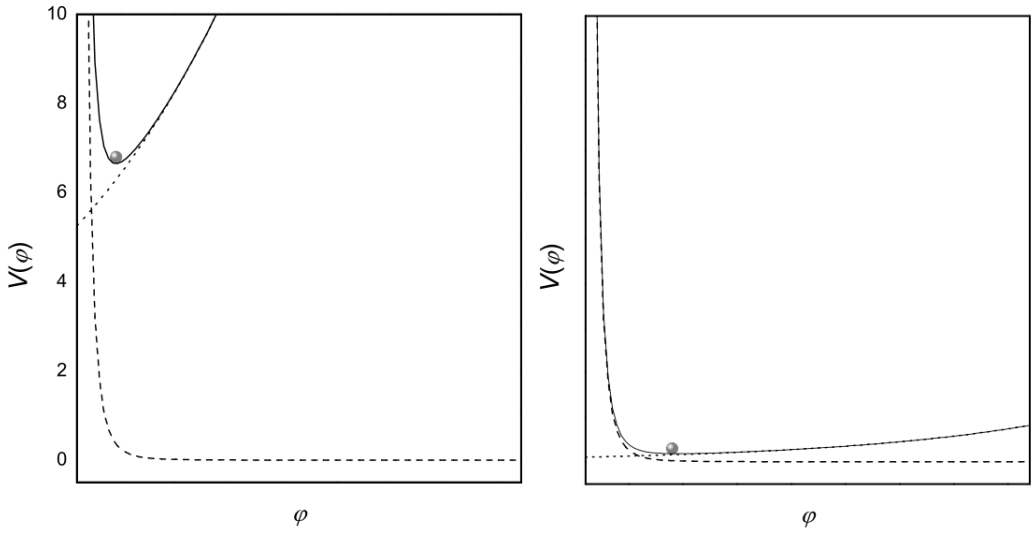


Figure 1: Plots illustrating the chameleon screening mechanism, [44]. The dashed, dotted and solid lines are the bare potential $V(\phi)$, the coupling function, and $V_{\rm eff}$ respectively. *Left Panel:* in high density regions, the minima of $V_{\rm eff}$ is close to $\phi = 0$ and $\vec{\nabla}\phi$ and hence the fifth force is small. *Right Panel:* in low density regions the fifth force can be non-trivial.

which is minimised at

$$\phi_{\rm min}^{n+1} = \frac{nV_0M_p}{\rho\beta}. \tag{2.12}$$

The mass of small fluctuations of the field around this minimum is

$$\begin{aligned} m^2(\rho) &= V_{\rm eff}(\phi,\rho)_{,\phi\phi}\,|_{\phi_{\rm min}} \\ &\approx \frac{\rho\beta}{M_p}\left[(n+1)\left(\frac{\rho\beta}{nV_0M_p}\right)^{\frac{1}{n+1}} + \frac{\beta}{M_p}\right] \end{aligned} \tag{2.13}$$

which, as required, increases monotonically with ρ.

Current constraints on chameleon models come from laboratory, cosmological, and astrophysical tests. Fifth force constraints from Eöt-Wash torsion-balance experiments [1] give the bound $M \lesssim 10^{-3}\,\text{eV}$, assuming β and n are of order one [15, 17, 45, 46]. Demanding that the Milky Way be screened gives a lower bound for the mass of the chameleon at cosmological densities, $m_{\rm cosm} \gtrsim 10^3 H_0$ or equivalently, $m_{\rm cosm}^{-1} \lesssim 1\,\text{Mpc}$, [17, 47]. Laboratory constraints restrict the mass at terrestrial densities to be $m_\oplus^{-1} \lesssim 50\,\mu\text{m}$ [49].

We can use (2.13) to translate constraints on the chameleon's cosmological or terrestrial mass to an estimate in regions with arbitrary density. Assuming $\beta \sim \mathcal{O}(1)$, we note that if we set V_0 by the dark energy scale, $M \sim 10^{-3}\,\text{eV}$, as indicated by the limits, then the first term inside of the square brackets in (2.13) will always dominate for $\rho \gtrsim \rho_{\rm cosm} \sim H_0^2 M_p^2$. This allows us to approximate the ratio of the chameleon's effective mass at two different densities as

$$\frac{m_a}{m_b} \sim \left(\frac{\rho_a}{\rho_b}\right)^{\frac{1}{2}\left(\frac{n+2}{n+1}\right)}. \tag{2.14}$$

We can therefore see that the strongest constraint comes from the laboratory experiments, and this is the bound we will use for the chameleon Compton wavelength. In our

Table 1: Order of magnitude bounds for the chameleon wavelength

Environment	Density	Compton wavelength upper bound	
		$n = 1$	n large
Earth	$\rho_\oplus \sim 10^{29}\rho_{\rm cosm}$	$10^{-5}\,$m	$10^{-5}\,$m
Accretion disc	$10^{-8}\rho_\oplus$	$10\,$m	$0.1\,$m
Galaxy	$10^{6}\rho_{\rm cosm}$	$10^{12}\,$m	$10^{7}\,$m

calculations it will be important to know whether the Compton wavelength of the chameleon is large or small compared to the size of the black hole. To facilitate this comparison, Table 1 gives a summary of the bounds for $m^{-1}(\rho)$ at the various densities we are interested in, obtained by rescaling the laboratory upper bound.

A solar mass black hole has a Schwarzschild radius of $\sim 10^3\,$m, while a supermassive black hole has $R_s \sim 10^{9-12}\,$m. Referring to Table 1, we see that the Compton wavelength of the chameleon will always be very small compared to the characteristic length scale of a black hole surrounded by an accretion disk. However, if there is no accretion disk and the black hole is simply surrounded by the ambient galactic density, the chameleon wavelength while potentially short compared to the size of a supermassive black hole, will be long compared to that of a stellar mass black hole. Interestingly, for the particular chameleon model we explore most fully in §3.1, which has $n = 4$, the Compton wavelength limit at galactic densities is of the same order (10^9m) as the radius of a typical supermassive black hole.

2.2 Environmentally dependent dilatons

Environmentally dependent dilaton models rely on a generalisation of the Damour-Polyakov mechanism, which arises in the strong coupling limit of string theory [48]. Their screening behaviour is a consequence of the fact that their coupling function has a minimum at some ϕ_d,

$$A(\phi) = 1 + \frac{a_2}{2M_p^2}(\phi - \phi_d)^2 + \dots \tag{2.15}$$

or

$$\beta(\phi) \equiv M_p \frac{\partial \ln A(\phi)}{\partial \phi} \approx \frac{a_2}{M_p}(\phi - \phi_d)\,. \tag{2.16}$$

The dilaton self-interaction potential is

$$V(\phi) = A^4(\phi)M^4 e^{-\frac{\phi}{M_p}} \equiv A^4(\phi)V_0 e^{-(\phi-\phi_d)/M_p} \tag{2.17}$$

where again we define $V_0 \equiv M^4 e^{-\phi_d/M_p}$ to simplify notation.

There is a caveat in that the action for dilatons contains a non-canonical kinetic term: $k^2(\phi)(\nabla\phi)^2$. The function $k(\phi)$ depends on the parameters of the particular string theory, but assuming that $\phi/M_p \ll 1$ it will generally take the form

$$k(\phi) \approx \lambda^{-1}\sqrt{1 + 3\lambda^2\beta^2(\phi)} \tag{2.18}$$

where λ typically falls in the range $\mathcal{O}(1) \lesssim \lambda \lesssim \frac{M_p}{M_s}$. Here, M_s is the string energy scale which we will take to be of order $10^{-1} - 10^{-2}M_p$. Thus our equation of motion is

$$\begin{aligned} \Box\varphi = k\Box\phi + k'\left(\nabla\phi\right)^2 &= V_{\rm eff,\varphi}\left(\varphi,\rho\right) = k^{-1}(\phi)V_{\rm eff,\phi}\left(\phi,\rho\right) \\ &\simeq k^{-1}(\phi)\frac{V_0}{M_p}\left[(4\beta(\phi)-1)A^4(\phi)e^{-(\phi-\phi_d)/M_p} + \beta(\phi)A(\phi)\frac{\rho}{V_0}\right] \end{aligned} \tag{2.19}$$

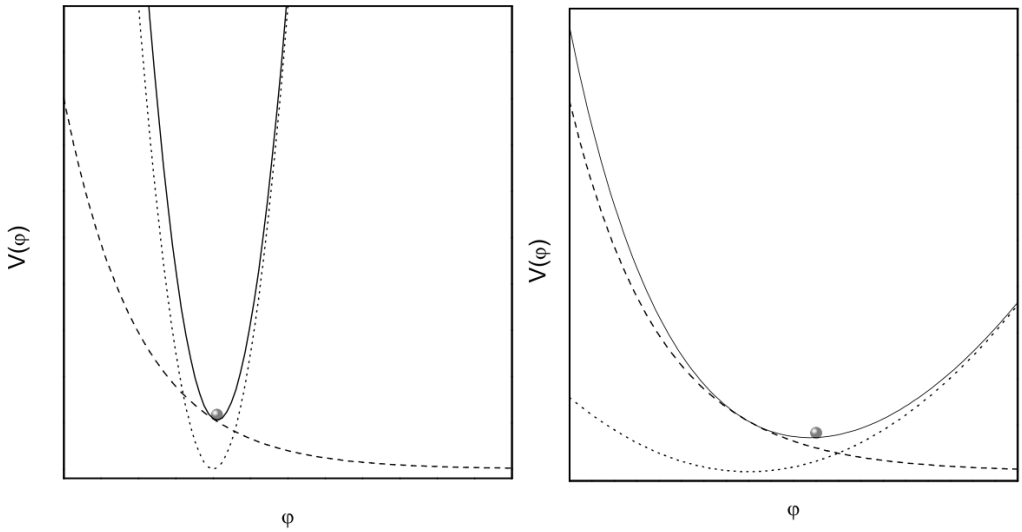


Figure 2: Plots illustrating the dilaton screening mechanism [51]. The dashed, dotted and solid lines are respectively the bare potential $V(\phi)$, the coupling function and $V_{\rm eff}$. *Left Panel:* in high density regions, the minima of $V_{\rm eff}$ is where the coupling strength vanishes and hence the fifth force is small. *Right Panel:* in low density regions the fifth force can be non-trivial.

where the redefined scalar, φ, is defined via $d\varphi = k(\phi)d\phi$.

The effective potential will be minimised when

$$\beta_{\rm min} \equiv \beta(\phi_{\rm min}) = \frac{V_0}{4V_0 + \rho A^{-3} e^{(\phi_{\rm min}-\phi_d)/M_p}} \simeq \frac{V_0}{\rho + 4V_0}, \tag{2.20}$$

for $\phi_{\rm min} \equiv \phi(\varphi_{\rm min})$. Thus, for large matter density, β is suppressed and the scalar field will decouple from matter. We also note that $0 < \beta \leq \frac{1}{4}$, so β is at most order unity for dilatons.

The mass of small fluctuations about $\varphi_{\rm min}$ is

$$\begin{aligned} m^2_{\varphi_{\rm min}} &= V_{{\rm eff},\varphi\varphi}\,|_{\varphi_{\rm min}} = \left.\frac{V_{{\rm eff},\phi\phi}}{k^2}\right|_{\phi_{\rm min}} \\ &\approx \frac{\lambda^2 V_0}{M_p^2}\frac{(12\beta^3_{\rm min} - 6\beta^2_{\rm min} + a_2)}{\beta_{\rm min}(1+3\lambda^2\beta^2_{\rm min})}. \end{aligned} \tag{2.21}$$

As with chameleons, the requirement that the Milky Way be screened places a lower bound on the mass of the dilaton at cosmological densities of $m_{\rm cosm} \geq 10^3 H_0$ [50]. This translates to the requirement that $\lambda^2 a_2 \gtrsim 10^5$. We note that because $0 < \beta \leq \frac{1}{4}$ and $a_2 \gg 1$, the dilaton's mass is dominated by the final term in the numerator, $m^2_{\varphi_{\rm min}} \sim \lambda^2 a_2(\rho + 4V_0)/M_p^2$. Saturating the bound on $\lambda^2 a_2$ gives an upper bound of $\mathcal{O}(10^{22})$m for the Compton wavelength of the dilaton in vacuum, which is always much larger than any black hole of astrophysical or cosmological interest. Meanwhile, in a denser region surrounding a black hole, the coupling function is markedly damped, see (2.20), resulting in the dilaton effectively decoupling from matter and being fixed very close to ϕ_d.

2.3 Symmetrons

Like dilatons, symmetrons exhibit screening behaviour because their coupling to matter goes to zero in dense regions, [12, 14, 52, 53]. They have a symmetry breaking potential and a

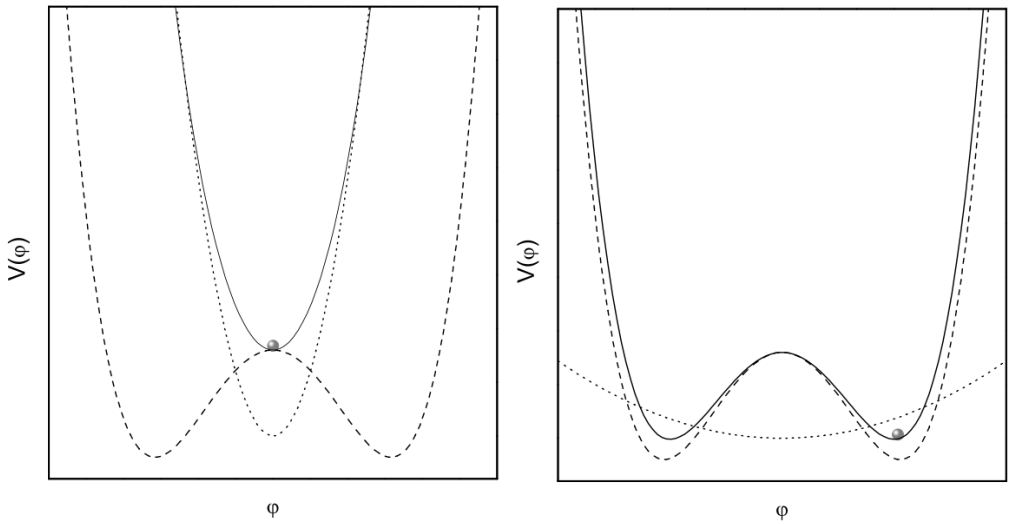


Figure 3: Plots illustrating the symmetron screening mechanism, [51]. The dashed, dotted and solid lines are the bare potential $V(\phi)$, the coupling function, and $V_{\rm eff}$ respectively. *Left Panel:* in high density regions, the minima of $V_{\rm eff}$ is where the coupling strength vanishes and hence the fifth force is small. *Right Panel:* in low density regions the fifth force can be non-trivial.

quadratic coupling function,

$$V(\phi) = -\frac{\mu^2}{2}\phi^2 + \frac{\lambda}{4}\phi^4, \qquad A(\phi) = 1 + \frac{a_2}{2M_p^2}\phi^2. \tag{2.22}$$

This gives the effective potential symmetry breaking properties which depend on the local matter density,

$$V_{\rm eff}(\phi, \rho) = \left(\frac{\rho a_2}{M_p^2} - \mu^2\right)\frac{\phi^2}{2} + \lambda\frac{\phi^4}{4}. \tag{2.23}$$

In regions with $\rho < \mu^2 M_p^2/a_2$, the symmetron will acquire a non-zero vacuum expectation value (VEV) of $\phi_{\rm min} = \pm\frac{\mu}{\sqrt{\lambda}}$. In these regions, the field couples to matter through $\beta(\phi) \approx a_2\phi_{\rm min}/M_p$ and will produce a fifth force. When ρ is large enough to restore symmetry, the VEV of ϕ vanishes, hence $\beta(\phi) \approx 0$ thus decoupling the symmetron from matter.

Note that though the screening behaviour does not depend on it, the effective mass of the symmetron will be different in regions of different density:

$$\text{for } \rho > \mu^2 M_p^2/a_2 \qquad m^2 \equiv V_{{\rm eff},\phi\phi}(\phi,\rho)|_{\phi=0} = \frac{\rho a_2}{M_p^2} - \mu^2 \tag{2.24}$$

$$\text{for } \rho < \mu^2 M_p^2/a_2 \qquad m^2 \equiv V_{{\rm eff},\phi\phi}(\phi,\rho)|_{\phi=\pm\frac{\mu}{\sqrt{\lambda}}} = 2\mu^2 \tag{2.25}$$

In order for symmetrons to produce long-range modifications of gravity, the effective potential should have spontaneously broken symmetry at cosmological densities, i.e., $\rho_{\rm cos} \sim H_0^2 M_p^2 \lesssim \mu^2 M_p^2/a_2$ and requiring the Milky Way to be screened imposes $a_2 \gtrsim 10^8$, [12], hence $\mu \gtrsim 10^4 H_0$ ($\mu^{-1} \lesssim 0.4\,{\rm Mpc}$). Additionally, for the symmetron to have effects comparable to gravity in low-density regions, we need $\beta(\phi_{\rm min}) \sim \mathcal{O}(1)$, which then requires λ to be very small: $\lambda \gtrsim 10^{24}(H_0/M_p)^2 \sim 10^{-96}$.

We can estimate an upper bound on the wavelength of the symmetron at arbitrary density by combining these constraints with (2.24). For regions with density greater than about $10^{-6}\,\mathrm{eV}^4$, the μ^2 term can be neglected, giving

$$m^{-1}(\rho) \lesssim \sqrt{\frac{\rho_{\cos}}{\rho}} \times \mathcal{O}(10^{22})\,\mathrm{m}. \tag{2.26}$$

Thus at physically realistic environmental densities, it is reasonable to assume that for symmetrons m^{-1} will be large compared to black hole systems.

3 Scalar profile of a black hole surrounded by matter

Our goal is to study whether a non-uniform matter distribution can induce a non-constant scalar field profile around a black hole and to estimate the magnitude of any scalar gradients which could potentially affect observable properties. Our approach will be to look for a static solution to the scalar field equation (2.8) on the Schwarzschild black hole geometry, together with a non-uniform matter distribution which is assumed (as with the scalar) not to back-react upon the geometry to this order. There are two aspects to this assumption. Firstly, on spatial scales over which the black hole curvature is significant, it requires that the curvature induced by the matter/scalar field be subdominant to that of the black hole. This translates roughly to the requirement

$$|T_\phi|,\ \rho \ll \frac{M_{BH}}{R_S^3} \approx \frac{M_p^6}{M_{BH}^2}. \tag{3.1}$$

Secondly, although on cosmological timescales we do expect the matter and scalar to have an effect on the spacetime geometry, this will involve a time evolution of order the Hubble scale, thus for the purposes of exploring observational consequences this is very much subdominant to local environmental timescales for the black hole, or reaction of the scalar field to the density profile[1]. Thus, the assumption of staticity is reasonable for timescales $\tau \ll H_0^{-1}$, which is safely the case for our astrophysical black holes.

One objection that might be raised to this approach is that the "no hair" theorems preclude any nontrivial scalar profile. The relevant no-hair theorem was explored by Sotiriou and Faraoni, [28], for the case of static and vacuum solutions. The essence of their argument is to take the scalar equation of motion (shown here for the Schwarzschild background), to multiply by $V_{,\phi}(\phi)\sqrt{g}$ and integrate:

$$\int_{2GM}^{\infty} \left\{ r^2 V_{,\phi}^2 + r(r-2GM)\phi' \frac{d}{dr}\left(V_{,\phi}\right) \right\} = \left[V_{,\phi} r(r-2GM)\phi' \right]_{2GM}^{\infty} = 0. \tag{3.2}$$

Clearly, if $V_{,\phi\phi} \geq 0$, as is the case with a wide range of physically relevant potentials, then the only possibility is that the integrand on the LHS is identically zero, i.e., $\phi' \equiv 0$, $\phi = \phi_{\min}$. Although at first sight the potentials we are considering appear to satisfy this constraint, we must be careful, as it is the effective potential that is the relevant quantity, and we are looking at a non-uniform environment where the matter density, ρ, jumps from being roughly zero to the ambient galactic or local accretion disc value. Thus, although $r^2 V_{,\phi}^2$ is positive definite, the derivative of $V_{,\phi}$ with respect to r contains a delta function, coming from the derivative of ρ. Combining this with the intuition that ϕ, if nontrivial, will tend to roll towards large values

[1] In [34], the time dependence of the back-reacted cosmological scalar plus black hole was shown to be at a timescale determined by the cosmological expansion, not the black hole light crossing time.

near the black hole horizon, we see that the second term in the integrand can potentially be very large and negative, thus ruling out a simple "no-hair" proof, and opening the possibility of a nontrivial scalar profile.

Before examining the system in detail, it is useful to first note how the scalar reacts to an arbitrary position-dependent matter distribution in the absence of a black hole. We take a spherically symmetric matter distribution, with a density (denoted by $\rho_\star$) approximately constant for large r. Let $\phi_\star$ be the value of the field that minimises the effective potential $V_{\rm eff}(\phi, \rho_\star)$. Following the procedure presented in [54], we expand the potential and coupling functions around $\phi_\star$. Defining $\delta\phi \equiv \phi - \phi_\star$, we have

$$V(\phi) = \sum_{n=0} \frac{V_n}{n!}(\delta\phi)^n \qquad \text{and} \qquad A(\phi) = \sum_{n=0} \frac{A_n}{n!}(\delta\phi)^n, \tag{3.3}$$

and hence the equation of motion becomes

$$\Box\delta\phi = (V_1 + \rho A_1) + (V_2 + \rho A_2)\,\delta\phi + (V_3 + \rho A_3)\,\frac{(\delta\phi)^2}{2} + \dots \tag{3.4}$$

This expression shows that a constant solution with $\phi = \phi_\star$ is only allowed if the $\delta\phi-$independent term on the right-hand side vanishes everywhere. If the density is constant with $\rho = \rho_\star$, this is automatically satisfied. For a non-uniform matter distribution, $\delta\phi = 0$ will be a solution only if

$$V_1 \equiv \left.\frac{\partial V(\phi)}{\partial\phi}\right|_{\phi_\star} = 0 \qquad \text{and} \qquad A_1 \equiv \left.\frac{\partial A(\phi)}{\partial\phi}\right|_{\phi_\star} = 0. \tag{3.5}$$

Using the potentials and coupling functions defined in Sections §2.1, §2.2, and §2.3, we can apply this analysis to chameleons, dilatons, and symmetrons. This gives:

$$\text{For chameleons:} \quad V_1 = -nM^{4+n}\phi_\star^{-(n+1)}, \qquad A_1 = \frac{\beta}{M_p}. \tag{3.6}$$

$$\text{For dilatons:} \quad V_1 = \frac{(4\beta(\phi_\star) - 1)}{k(\phi_\star)}\frac{M^4}{M_p}, \qquad A_1 = \frac{\beta(\phi_\star)}{k(\phi_\star)M_p}. \tag{3.7}$$

$$\text{For symmetrons:} \quad V_1 = 0, \qquad A_1 = \frac{a_2\phi_\star}{M_p}. \tag{3.8}$$

Note that for dilatons we have performed the expansion in term of the redefined field φ where $d\varphi = k(\phi)d\phi$, using the definition $\phi_\star \equiv \phi(\varphi_\star)$. Also, we have kept only the leading order terms in ϕ/M_p, writing $A(\phi_\star) \approx 1$ and $e^{-\phi_\star/M_p} \approx 1$.

From these expressions we see that in the vicinity of a non-uniform distribution of matter, chameleons and dilatons are not only expected, but in fact are required to take on a non-constant scalar profile. This will also be the case for symmetrons if the density far from the black hole is low enough to put the effective potential in its symmetry-breaking phase, with $\phi_\star = \pm\frac{\mu}{\sqrt{\lambda}}$. However, if $\rho_\star$ is large enough $\phi_\star = 0$ for symmetrons, so the trivial solution is allowed. This means that symmetrons can (but are not required to) take on a configuration which is identical to that of general relativity.

Turning now to the case of the black hole, our setup is motivated by a physical picture of an astrophysical black hole, typically located within some larger distribution of matter. Although astrophysical black holes will be rotating, for the purpose of establishing whether

or not a nontrivial scalar profile is possible, it will suffice to consider a purely monopole spherically symmetric set-up, in which the black hole is descibed by the Schwarzschild metric:

$$ds^2 = -\left(1 - \tfrac{R_s}{r}\right) dt^2 + \left(1 - \tfrac{R_s}{r}\right)^{-1} dr^2 + r^2 d\Omega^2 \,, \tag{3.9}$$

(denoting $R_s = 2GM$ for clarity), and the density profile by

$$\rho(r) \equiv \begin{cases} 0 & R_s < r < R_0 \text{ (Region I)} \\ \rho_\star & r > R_0 \text{ (Region II)} \end{cases} \tag{3.10}$$

The motivation for this profile is that the larger distribution of matter in which the black hole sits will be characterised by a density $\rho_\star$ (taken to be constant in (3.10)), which is assumed to vary slowly on length scales comparable to the size of the black hole. Very close to the black hole however, we expect an approximately empty inner region, motivated by the fact that all black holes have an innermost stable circular orbit (ISCO – e.g. at $3R_s$ for the Schwarzschild black hole), inside of which all massive particles fall into the black hole on a relatively short time-scale. We therefore treat the density inside some inner radius, R_0 as being roughly zero. Our matter profile (3.10) can thus be viewed as a crude model of either a *spherically symmetric* accretion "disk" or a galactic "halo" where the matter inside R_0 has fallen into the black hole.

Using this model, and taking $\phi = \phi(r)$, the scalar field equation becomes an ordinary differential equation:

$$\Box\phi = \frac{1}{r^2}\frac{d}{dr}\left[r^2\left(1 - \frac{R_S}{r}\right)\frac{d\phi}{dr}\right] = \frac{\partial V_{\rm eff}(\phi,\rho)}{\partial\phi}. \tag{3.11}$$

The external matter distribution sets the asymptotic boundary condition $\phi \to \phi_\star$, where $V_{\rm eff}(\phi,\rho_\star)_{,\phi}\big|_{\phi_\star} = 0$. Note that we typically expect $\phi(r)$ to approach this minimum over a length scale characterised by $m_\star^{-1}$, where $m_\star \equiv V_{\rm eff}(\phi,\rho_\star)_{,\phi\phi}\big|_{\phi_\star}$.

We now solve this scalar equation of motion for chameleons §3.1, dilatons §3.2, and symmetrons §3.3, respectively. Note that although we expect $R_0 \simeq R_{\rm ISCO} = 3R_s$ for the Schwarzschild black hole, to make our analytic calculations tractable we will often use the approximation $R_s/R_0 \ll 1$. While the actual value of 1/3 means there will be quantitative inaccuracy to the analytic expressions, we nonetheless expect that the qualitative picture emerging from our analytic results will be correct.

3.1 Chameleon profile

Here we show that the presence of a non-uniform matter density sources variations in the chameleon field, endowing the black hole with a scalar profile. We first derive an analytic approximation to the scalar profile, and derive the horizon value of the chameleon in two limits: where the scalar Compton wavelength is either very large or very small compared to the size of the black hole. As we saw in Section 2.1, if we take $\rho_\star$ to be the density of an accretion disk, $m_\star R_0$ will always be large ($\gg 1$). If $\rho_\star$ is the density of a galactic halo the chameleon will have $m_\star R_0 \ll 1$ for stellar mass black holes, and $m_\star R_0 \lesssim 1$ for supermassive black holes. Thus, both limits will potentially be relevant for chameleons. We then present numerical solutions for a range of chameleon model data, comparing them to the derived analytic approximations.

Analytic analysis

In order to both explore analytic approximations and perform numerical integrations, we rewrite the chameleon equation of motion in terms of dimensionless variables:

$$\hat{\phi} = \frac{\phi}{\phi_\star} \ , \quad x = \frac{r}{R_s} \ , \quad \hat{m}^2 = m_*^2 R_s^2 = (n+1)\frac{\rho_* \beta R_s^2}{M_p \phi_*} \tag{3.12}$$

giving

$$\hat{\phi}'' + \frac{2x-1}{x(x-1)}\hat{\phi}' = \frac{x}{(x-1)}\frac{\hat{m}^2}{(n+1)}\left[\Theta[x-x_0] - \frac{1}{\hat{\phi}^{n+1}}\right] \tag{3.13}$$

The physical set-up is that we have a dense extended region (II) in which the chameleon will be held essentially constant at ϕ_*. Nearer to the black hole, we have a region of vacuum (region I) in which the chameleon is allowed to roll freely and is only restricted by the dimension of region I. For a low mass chameleon (large Compton wavelength with respect to the black hole) we do not expect the chameleon to change much from its asymptotic value, hence we can perform an analytic approximation assuming a small change in $\hat{\phi}$. For large mass chameleons however, we do expect a rather sharp and rapid response to the vacuum region, and for the chameleon to have something analogous to a thin shell with a power law behaviour, commensurate with the rolling of the vacuum potential. Thus, for our analytic approximation we also use a different expression in region I for large masses. In both cases in region II however, the field will fall off to its asymptotic value, and we expect $\hat{\phi} \simeq 1 + \delta\hat{\phi}$, where

$$\delta\hat{\phi} \simeq C\frac{e^{-\hat{m}(x-x_0)}}{x^{1+\hat{m}/2}} \tag{3.14}$$

for some constant C.

• $\hat{m}x_0 \ll 1$

For a long range chameleon field, we expect that $\hat{\phi}$ will not vary much, and assume the change in $\hat{\phi}$ in region I is dominated by the geometry, i.e.

$$\left[x(x-1)\hat{\phi}'\right]' = -\frac{\hat{m}^2 x^2}{(n+1)\hat{\phi}_h^{n+1}}\left(1 + \mathcal{O}(\delta\hat{\phi}/\hat{\phi}_h)\right) \ , \tag{3.15}$$

which gives the solution:

$$\hat{\phi} = \hat{\phi}_h - \frac{\hat{m}^2}{6(n+1)\hat{\phi}_h^{n+1}}[x^2 + 2x + 2\ln x - 3] \, . \tag{3.16}$$

Matching the solutions at x_0 with the asymptotic form (3.14) gives

$$\begin{aligned} \hat{\phi}_h &= 1 + \frac{\hat{m}^2}{6(n+1)\hat{\phi}_h^{n+1}}\left[x_0^2 + 2x_0 + 2\ln x_0 - 3 + \frac{4x_0^2 + 4x_0 + 4}{2\hat{m}x_0 + 2 + \hat{m}}\right] \\ C &= \frac{\hat{m}^2}{3(n+1)\hat{\phi}_h^{n+1}}\frac{x_0^{1+\hat{m}/2}(x_0^2 + x_0 + 1)}{\hat{m}x_0 + 1 + \hat{m}/2} \ . \end{aligned} \tag{3.17}$$

Writing $\hat{\phi} = 1 + \delta\hat{\phi}$, and expanding to leading order gives:

$$\hat{\phi} \simeq 1 + \begin{cases} \frac{\hat{m}^2}{6(n+1)}\left[3x_0^2 - x^2 + 4x_0 - 2x + 2 + 2\ln\frac{x_0}{x}\right] & x < x_0 \\ \frac{\hat{m}^2}{3(n+1)}\left(x_0^2 + x_0 + 1\right)\frac{x_0}{x}e^{-\hat{m}(x-x_0)} & x > x_0 \end{cases} \tag{3.18}$$

We are mainly interested in the horizon value of the chameleon field, and how this differs from the asymptotic value, as this indicates the impact of the black hole on the local scalar profile, and we can read this off to leading order in $\hat{m}x_0$ as:

$$\hat{\phi}_h \approx 1 + \frac{\hat{m}^2 x_0^2}{2(n+1)}\,, \tag{3.19}$$

or,

$$\delta\phi_h \approx \frac{\rho_\star \beta R_0^2}{2M_p}. \tag{3.20}$$

Here we see that $\delta\phi_h$ increases with the coupling function β, the density of the local environment and the range in which the chameleon can roll (R_0).

• $\hat{m}x_0 \gg 1$

In the case that the chameleon is short range, we can use the same simple approximation presented above, although without expanding (3.17) near $\hat{\phi} = 1$. This approximation should give a good order of magnitude estimate for $\hat{\phi}_h$, however for later purposes we want a better approximation to the field profile so we can estimate ϕ'. Since we expect the key feature of the profile to be the rapid roll of the chameleon near the boundary of the two regions, we focus on the change in $\hat{\phi}$ being dominated by the potential:

$$\hat{\phi}'' \simeq -\frac{\hat{m}^2}{(n+1)}\frac{1}{\hat{\phi}^{n+1}} \tag{3.21}$$

which is solved by

$$\hat{\phi} \simeq 1 + \left[\frac{\hat{m}^2(n+2)^2(x_1-x)^2}{2n(n+1)}\right]^{1/(n+2)}. \tag{3.22}$$

Meanwhile, matching to (3.14) at x_0 gives:

$$\hat{\phi} \simeq 1 + \begin{cases} \left[\frac{\hat{m}^2(n+2)^2}{2n(n+1)}\right]^{\frac{1}{n+2}} \left(x_0 - x + \frac{2}{(n+2)\hat{m}}\right)^{\frac{2}{n+2}} & x < x_0 \\ \left[\frac{2}{n(n+1)}\right]^{\frac{1}{n+2}} \left(\frac{x_0}{x}\right)^{1+\hat{m}/2} e^{-\hat{m}(x-x_0)} & x > x_0 \end{cases} \tag{3.23}$$

This profile captures a rapid transition to large near horizon values, although it does not solve the equations of motion at the horizon, as it has been tailored to the variation near x_0. In spite of this, as we will see from the numerical work, it does indeed capture the essential features of the field profile (see next subsection). Indeed, both this expression, and the simpler geometry dominated approximation data (3.17) give the same dependence of the horizon value on x_0 and $\hat{m}$ to leading order in x_0

$$\hat{\phi}_h \approx \hat{\phi}_c \left(\frac{\hat{m}^2 x_0^2}{(n+1)}\right)^{\frac{1}{n+2}}, \tag{3.24}$$

where $\hat{\phi}_c^{n+2} = (n+2)^2/(2n)$ for the potential dominated expression, and $1/6$ for the geometry dominated expression. Re-expressing in terms of the dimensionful variables gives

$$\phi_h \propto \left((n+2)^2 V_0 R_0^2\right)^{\frac{1}{n+2}}. \tag{3.25}$$

This result shows how the value of the chameleon is dependent on the parameters of the model: Making the chameleon self-interaction potential $V(\phi)$ steeper by lowering n or raising V_0 will drive ϕ_h to larger values, as will increasing R_0.

In both cases, the field is close to its asymptotic value in region II, and rolls to larger values of ϕ in region I. For the long range chameleon, we expect our analytic approximation to be very good and accurate up to sub-leading dependence on x of order $\hat{m}/x_0$. For the short range chameleon, we could not find a simple analytic expression that worked throughout region I: the potential dominated expression should work well near x_0, however, the effect of the nearing event horizon should modify this profile once we are at smaller x. Both approximations gave the same form for the horizon value of the chameleon however, therefore we expect the actual profile to have features of both, and certainly to be nontrivial!

For both small and large mass chameleons, increasing the size of the empty region around the black hole (thus giving the chameleon more 'space' to roll) increases ϕ_h. We can read this as a rough restatement of a no-hair theorem, noting that as we take $R_0 \to \infty$ the requirement that the scalar stay finite is violated.

Numerical Results

Although the analytic results presented are strongly suggestive of the existence of a nontrivial scalar profile around the black hole, to confirm that they are capturing the essence of the actual scalar solution, we must verify that the asymptotic expansions do indeed correspond to full solutions. We have therefore integrated (3.13) numerically for a range of parameters of $\hat{m}$, n, and x_0 using a gradient flow algorithm. In all cases the field profile shows a response to the black hole as expected, and we present a selection of our results in figures 4–6 demonstrating the qualitative nature of the field profiles, comparing them to the analytic approximations, and summarizing the horizon data dependence on the model parameters

In figure 4 we show the profile of the chameleon field over a wide mass range for $R_0 = 3R_s$ and $n = 4$ (the picture is similar for different R_0 and n). The numerical solutions show how the profile of the scalar changes qualitatively between small and large masses. The low mass scalars remain close to their asymptotic value, and have a fairly smooth profile. The large mass scalars on the other hand have a much sharper fall-off as we approach the dense region, cutting off very strongly at R_0. This is reminiscent of the "thin shell" behaviour, [10], which occurs around a massive object. The main difference here is that it is our exterior region which is dense, with the chameleon relaxing to its new VEV in the interior. The fact that the field has a significant variation as it nears R_0 is anticipated by our analytic approximation, although is severely underestimated by the simple geometric approximation used for lower masses (as seen in comparing the analytic and numerical solutions in figure 5).

In figure 5 we compare our analytic approximations to the numerical data. We show sample plots for $\hat{m} = 0.1$ and $\hat{m} = 1000$, taking $R_0 = 3R_s$ and $n = 4$ as before. In both cases we compare the numerical data to the analytic approximation given by (3.14), (3.16) with the exact expressions from (3.17). For the large mass plot, we also show what we expect to be the more accurate approximation, (3.23), derived by assuming the dominance of the potential. The approximations are seen to be extremely accurate in tracking the shape of the chameleon profile. The small mass approximation is accurate to better than 1%. The large mass plot is accurate near R_0 (where it was tailored to be), but since $R_0/R_s = 3$, the effect of the geometry rapidly starts to make itself felt, leading to an overshoot of this approximation

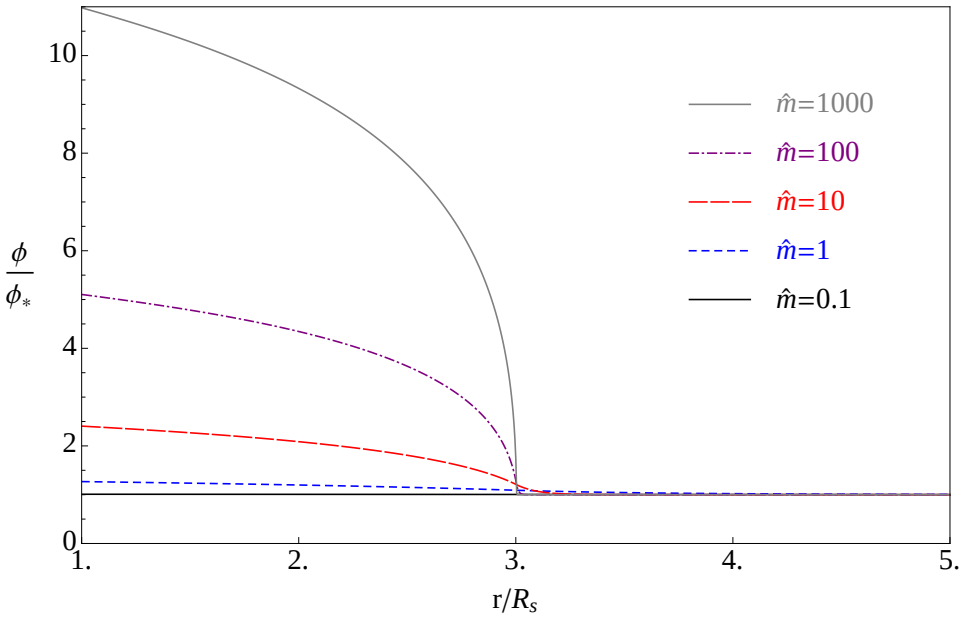


Figure 4: Plots of numerical solutions for the chameleon field for a range of values of the chameleon mass $\hat{m} = m_\star R_s$. The differing behaviour for the large and low mass solutions is demonstrated.

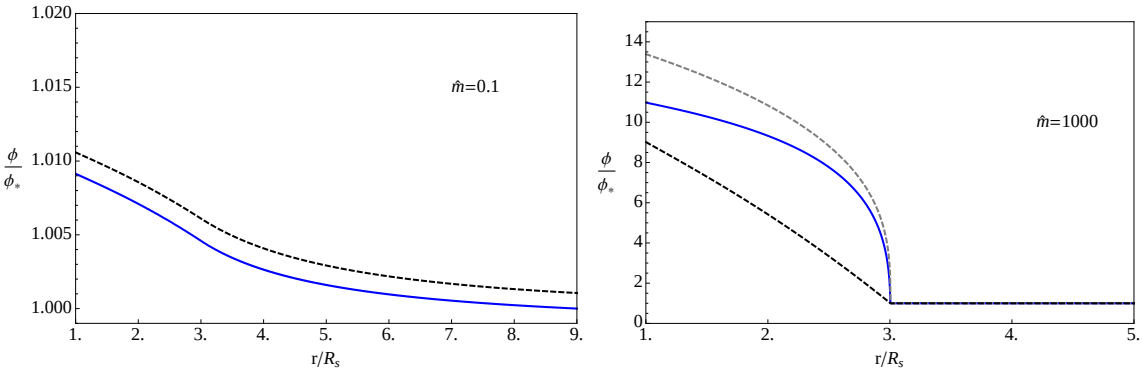


Figure 5: A comparison of the analytic approximations to the numerical solution (in blue) at both small and large mass. The dashed black line is the full analytic approximation, given by (3.14), (3.16) with the exact expressions from (3.17). For the large mass case, the gray line is the potential dominated expression, which better captures the shape of the chameleon profile.

at the horizon. However, it can be seen to be a far better fit than the geometry dominated expression which works so well for small masses.

Finally, in figure 6 we compare the horizon values of the chameleon over a range of masses and the potential index n. We show the numerical horizon data, the analytic data obtained by solving (3.17), and the small/large mass, large x_0 leading order approximations to this horizon value. In both plots R_0 is fixed at $3R_s$, and $n = 4$ for varying $\hat{m}$. In spite of the shortcomings of the analytic approximations, these plots show that the analytics pick up the essential dependence of the chameleon field. Indeed, it is surprising just how good the rough value is at extracting the main dependence of the horizon chameleon data on the model parameters.

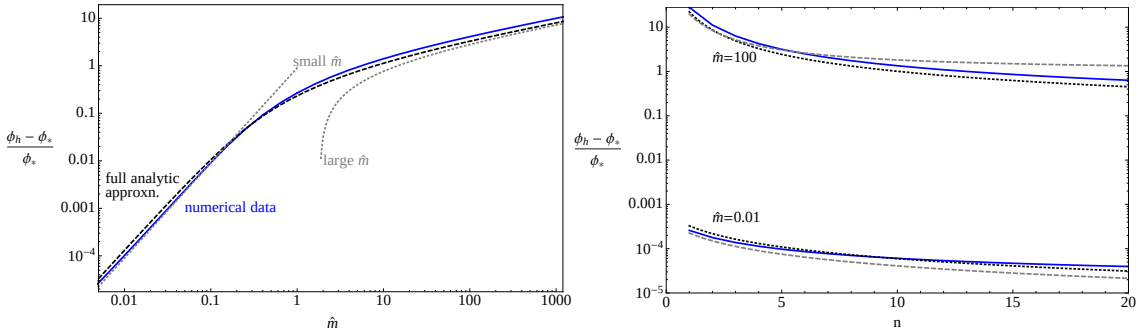


Figure 6: The horizon value of the chameleon field as a function of $\hat{m}$ and n, shown for comparison against the analytic approximations. The left plot shows the variation with $\hat{m}$, and the right the variation with n. The numerical data is plotted in blue, the full analytic approximation value in dotted black, and the leading order approximations in dashed grey. In varying n, we compare at both large and small masses.

3.2 Dilaton profile

Environmentally dependent dilatons will also have a non-constant profile. Recall that the dilaton kinetic term has a coupling factor $k(\phi)$, so that the equation of motion for the dilaton is

$$\frac{1}{r^2}\left[r(r-1)\phi'\right]' = -\frac{3\lambda^2\beta\beta'}{1+3\lambda^2\beta^2}\phi'^2 + \frac{1}{k^2}V_{\text{eff},\phi}(\phi,\rho) \tag{3.26}$$

where

$$\frac{1}{k^2}V_{\text{eff},\phi}(\phi,\rho) = \frac{V_0\lambda^2}{M_p(1+3\lambda^2\beta^2)}\left[(4\beta-1)A^4 e^{-(\phi-\phi_d)/M_p} + \beta A\frac{\rho}{V_0}\right] \tag{3.27}$$

In region I, $\rho \simeq 0$, and hence our vacuum dilaton value is $\beta = 1/4 \Rightarrow \phi_0 = \phi_d + M_p/4a_2$, with a mass $m_0^2 \simeq 4a_2V_0/M_p^2$. In region II, we have instead a small coupling function, $\beta = V_0/(\rho_* + 4V_0)$, and $\phi_* \simeq \phi_d + M_pV_0/a_2\rho_*$ with $m_*^2 \simeq bm_0^2$, where $b = (\phi_0 - \phi_d)/(\phi_* - \phi_d) \simeq \rho_*/4V_0$. In other words, we have a hierarchy between the two regions set by the ratio of the local accretion disc or galactic energy density ρ_*, and the background potential scale (taken to be the cosmological density), V_0. Inputting the parameter values $a_2 \simeq 10^5$, $V_0 \sim \rho_{\text{cosm}}$, we see $m_0^2R_s^2 \sim 10^{-40} - 10^{-28}$ for astrophysical / supermassive black holes, hence the scalar field is extremely light in region I. In region II, the coupling function is extremely small, hence we expect ϕ to be very close to its minimum ϕ_*. Thus for the dilaton, we expect a low mass or long range approximation to be appropriate in any analytical analysis.

Analytic analysis for the dilaton

Proceeding analogously to the chameleon, we introduce a new field variable

$$y = \frac{\phi - \phi_d}{\phi_* - \phi_d}\,, \tag{3.28}$$

where we expect $(y-1) \ll 1$, hence $\lambda y \ll b$ (recall $b = \rho_*/\rho_{\text{cos}}$), and our equation of motion is well approximated by

$$y'' + \frac{2x-1}{x(x-1)}y' = \frac{\hat{m}^2x}{x-1}\left[\Theta[x-x_0](b-1)y + (y-b)\right] \tag{3.29}$$

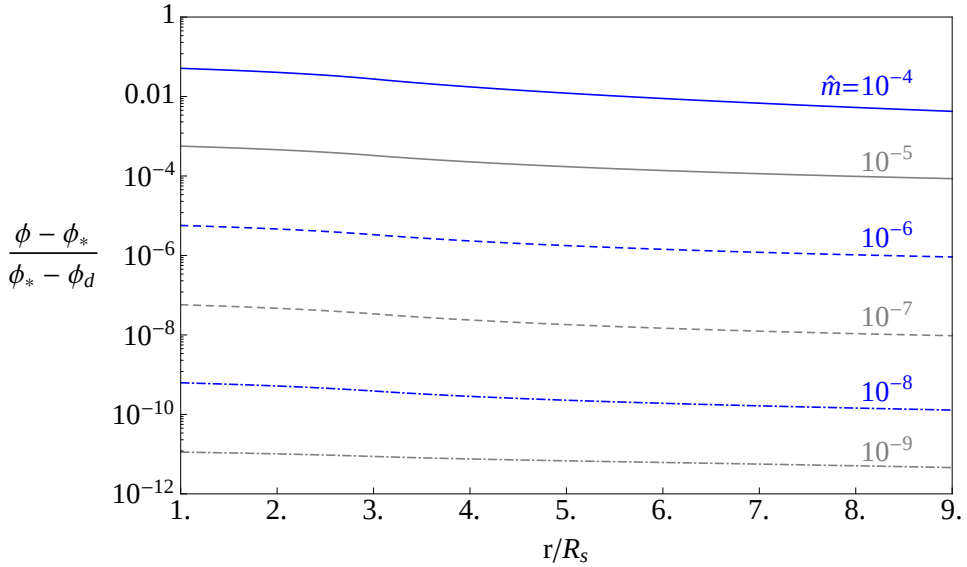


Figure 7: A plot of the variation of the dilaton field near the black hole, shown for a range of masses. The profile of the dilaton remains similar, with the horizon value dropping as $\hat{m}^2$.

where we have set $\hat{m}^2 = \lambda^2 m_0^2 R_s^2$. Clearly $\hat{m}^2, \hat{m}^2 b \ll 1$, and hence our dilaton field will remain close to $y = 1$ throughout regions I and II. We therefore take $y = 1 + \delta y$, and approximate our solutions in each region with the horizon and asymptotic expansions:

$$y = 1 + \begin{cases} \delta y_h + \frac{\hat{m}^2}{6}(1 + \delta y_h - b)[x^2 + 2x + 2\ln x - 3] & x \leq x_0 \\ C\, x^{-(1+\hat{m}\sqrt{b}/2)}\, e^{-\hat{m}\sqrt{b}(x-x_0)} & x \geq x_0 \end{cases} \tag{3.30}$$

where the constants C and δy_h are given by matching at x_0. Keeping terms only to leading order in $\hat{m}^2 b$ gives:

$$\begin{aligned} \delta y_h &= \frac{\hat{m}^2}{6}(b-1)\,(3x_0^2 + 4x_0 + 2\log x_0 - 1) \\ C &= \frac{\hat{m}^2}{3}(b-1)x_0(1 + x_0 + x_0^2)\,. \end{aligned} \tag{3.31}$$

We see therefore that the shift in the dilaton value at the horizon of the black hole is roughly $\hat{m}^2 b x_0^2/2$.

Numerical results

Numerically, it is rather difficult to explore the extremely small mass parameter values relevant for the dilaton directly with our simple techniques, however, by comparing numerical data with analytic profiles for a range of less tiny (though still small) masses, we can verify the analytic understanding, and extrapolate our results to the mass ranges of relevant for the dilaton. We therefore integrated (3.29) numerically for masses ranging from $10^{-4} - 10^{-14}$, taking again $R_0 = 3R_s$.

In figure 7 we show a plot of the variation of the dilaton field over a wide range of orders of magnitude in the mass. The profile is confirmed to be a gentle, small variation from the asymptotic value, and drops a couple of orders of magnitude for each order of magnitude drop in $\hat{m}$ as expected.

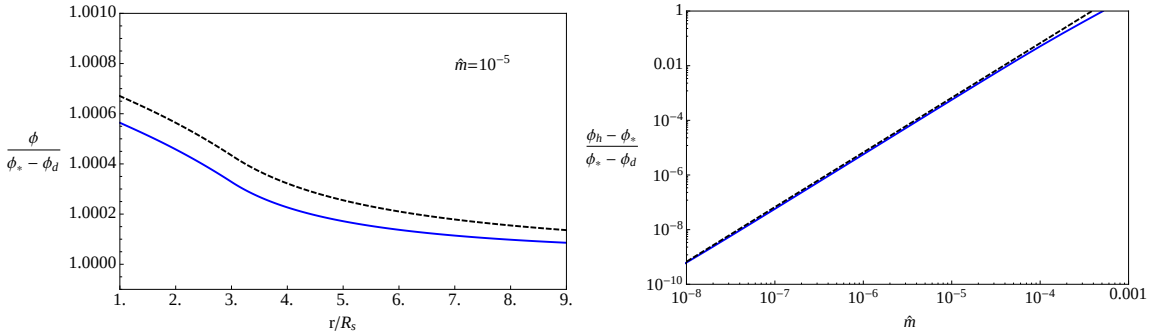


Figure 8: A comparison of the analytic approximation to the numerical solutions: *Left:* A plot of the field profile obtained numerically for $\hat{m} = 10^{-5}$ compared to the analytic approximation. *Right:* The horizon value of the dilaton field as a function of $\hat{m}$, shown for comparison against the analytic result.

In figure 8, we compare the numerical and analytic solutions as before by plotting an explicit profile (here chosen at $\hat{m} = 10^{-5}$), and the horizon data as a function of mass, again comparing the numerical, and analytical approximations. As with the chameleon, there is an excellent agreement in the two expressions, with the horizon data in particular giving almost indistinguishable results over a wide range of orders of magnitude for $\hat{m}$, therefore we see no reason to doubt the extrapolation of the data to much smaller masses, or other model parameters.

3.3 Symmetron profile

The symmetron field is distinct from the dilaton and chameleon in its behaviour, as the screening occurs due to dense regions restoring symmetry in the coupling function, driving it to zero:

$$\frac{r - R_s}{r}\phi'' + \frac{2r - R_s}{r^2}\phi' = \frac{\rho a_2}{M_p^2}\phi - \mu^2\phi + \lambda\phi^3 \,. \tag{3.32}$$

In region II, the density $\rho_\star$ is large enough so that $\langle\phi\rangle = 0$ at its minimum, whereas in region I, $\langle\phi_{\rm vac}\rangle = \pm\mu/\sqrt{\lambda}$. Whether or not the symmetron can develop a nontrivial profile therefore becomes an issue of the tachyonic instability of the false vacuum $\langle\phi\rangle = 0$ in region I, which is always a solution to the symmetron equation of motion (3.32). In order for ϕ to develop a nonzero profile, there has to be sufficient space for a fundamental mode of the wave equation to exist within region I, roughly of order the Compton wavelength of the symmetron. Given that we take $R_0 = 3R_s$, this translates to $\mu R_s \gtrsim \mathcal{O}(1/3)$ or so. Given that we expect $\mu^{-1} \sim$Mpc, we are clearly well outside this régime for any cosmologically relevant symmetron, therefore our analysis will focus on confirming this intuition, and demonstrating the existence and magnitude of this limit.

Analytic approximations for the symmetron

Writing $x = r/R_s$ as usual, $\hat{\phi} = \sqrt{\lambda}\phi/\eta$, $\hat{\mu} = \mu R_s$, and $\hat{m}^2 = \rho_* a_2 R_s^2/M_p^2 - \hat{\mu}^2$, the equation of motion becomes:

$$\left[x(x-1)\hat{\phi}'\right]' = x^2\hat{\phi}\left[\hat{m}^2\Theta(x - x_0) - \hat{\mu}^2\Theta(x_0 - x)(1 - \hat{\phi}^2)\right] \,. \tag{3.33}$$

For small mass parameters, we might expect a small variation in our scalar field, therefore we try our usual approximate solution for a slowly varying field,

$$\hat{\phi} = \begin{cases} \hat{\phi}_h - \frac{\hat{\mu}^2}{6}\hat{\phi}_h(1-\hat{\phi}_h^2)\left[x^2+2x+2\log x-3\right] & x \le x_0 \\ C\,\frac{e^{-\hat{m}(x-x_0)}}{x^{-(1+\hat{m}/2)}} & x \ge x_0\,. \end{cases} \tag{3.34}$$

However we now see something interesting arising in our matching conditions:

$$\begin{aligned} \frac{C}{x_0^{1+\hat{m}/2}} &= \hat{\phi}_h\left[1-\frac{\hat{\mu}^2}{6}(1-\hat{\phi}_h^2)(x_0^2+2x_0+2\log x_0-3)\right] \\ &= \frac{\hat{\mu}^2}{3}\hat{\phi}_h(1-\hat{\phi}_h^2)\frac{(x_0^2+x_0+1)}{(\hat{m}x_0+1+\hat{m}/2)} \end{aligned} \tag{3.35}$$

$\hat{\phi}_h$ now scales out of these relations, and we see that $(1-\hat{\phi}_h^2) \simeq \frac{6}{\hat{\mu}^2 x_0^2} \le 1$. Clearly this is inconsistent for small $\hat{\mu}$, therefore our approximation indicates that there should be a lower bound on the mass for which a symmetron solution can exist (in keeping with our earlier intuition), and gives the mass limit as $\hat{\mu}^2 x_0^2 \lesssim 6$.

For large masses, where we would expect $\hat{\phi}$ to approach close to unity very rapidly inside region I, the approximation we use to get the interior solution in (3.34) is not reliable, as $\hat{\phi}$ is varying significantly. With the chameleon, we approximated our profile by taking the potential to dominate the behaviour of the scalar, for the symmetron, provided $x_0\hat{\mu}$ is large enough, our differential equation is well approximated by the $\lambda\phi^4$ kink model – and our field will take on a tanh profile as it makes the transition to its new, true, vacuum. We can therefore take the approximation

$$\hat{\phi} \simeq \begin{cases} \tanh\left(\frac{\hat{\mu}(x_0+\delta x-x)}{\sqrt{2}}\right) & x < x_0 \\ \tanh\left(\frac{\hat{\mu}\,\delta x}{\sqrt{2}}\right)\left(\frac{x_0}{x}\right)^{1+\hat{m}/2} e^{-\hat{m}(x-x_0)} & x > x_0 \end{cases} \tag{3.36}$$

which rapidly transitions from 0 to 1 in a thin shell inside region I.

Obviously, these arguments are only suggestive, and in no way constitute a proof of the nonexistence of a nontrivial solution at low mass, however, they are consistent with our numerical findings, and also with the results of [54]. Indeed, studying our black hole model in the context of the analysis of spontaneous scalarization in [54], we again find that at low masses the black hole is not required to have a nontrivial symmetron profile.

Numerical results for the symmetron

As previously noted, the mass of the symmetron is well below the expected threshold for a nontrivial field profile, therefore our numerical investigation focussed on the confirmation of the analytical picture presented above. We took $R_0 = 3R_s$ as usual, and explored a range of masses around unity, $\hat{\mu}^2 \sim 0.5-5$, to cover the régime in which we expect the symmetron field switches on in the vicinity of the black hole.

The results presented in figures 9 and 10 were computed for a galactic density environment, $\rho/V_0 \sim 10^6$, however the system is insensitive to an increase in density of region II, as the key physics here is that the coupling function to matter has switched off, fixing the symmetron at its (local) vacuum value.

Figure 9 shows the profile of the symmetron gradually switching on as the effective mass in the vacuum of region I is raised. The transition of the horizon value of the symmetron

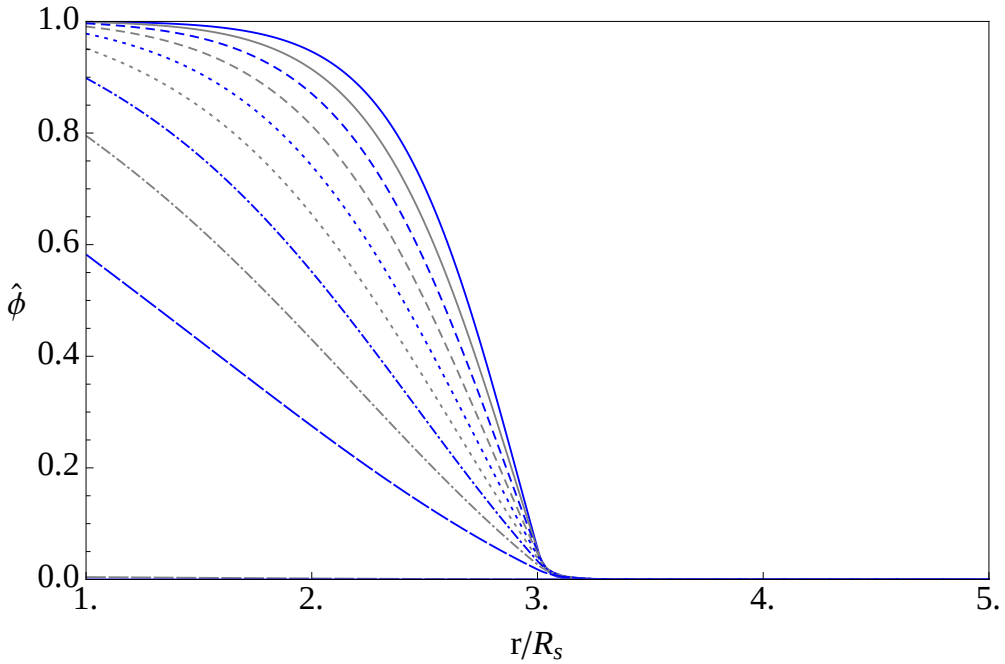


Figure 9: The symmetron profile for a sequence of masses from $\sqrt{5}$ to $1/\sqrt{2}$: $\hat{\mu}^2 = 5 \times 10^{-i/10}$ for $i = 0, 1, ...10$. This range covers the switching off of the symmetron in region I, and the final profile can just be detected on the $x-$axis.

from zero to unity as the mass is increased is seen to occur rather rapidly, and is shown in more detail in figure 10. The key point from figure 9 is that the intuition of a cut-off in mass for a nontrivial symmetron profile is confirmed.

In figure 10, we explore the correspondence between the analytic analysis and the numerical data. First, the phase transition of the horizon value of the symmetron as a function of inverse mass is shown in comparison to the low mass analytic approximation, $\sqrt{1 - 6/\hat{\mu}^2 x_0^2}$. The cut-off in the symmetron profile is seen to be quite sharp, and unsurprisingly the low mass analytic approximation does not track the initial drop in the horizon value at larger masses that well, although it is very accurate at predicting the switch-off of the symmetron. Secondly, the field profile of a larger mass ($\hat{\mu} = \sqrt{5}$) symmetron is shown for comparison against the tanh profile of the analytic guess. Here, the correspondence between the analytic approximation and the actual profile is amazingly good and shows the analytic work is capturing the essence of the actual physics very well.

4 Observational implications

In the previous section we studied static, spherically symmetric solutions of the scalar field equation on a background comprising a Schwarzschild black hole and a static, spherically symmetric, constant matter distribution. Having shown that chameleons and dilatons produce a solution which is distinct from GR, we would now like to know whether they might have observable effects.

In our static model, the black hole is not moving through the scalar gradient and $\phi_\star$ is constant, so on its own it will not emit scalar radiation through the mechanisms explored in [55] and [56]. However, as the presence of a non-zero scalar gradient will cause matter particles to feel a fifth force, we can comment on how chameleon and dilaton hair will affect

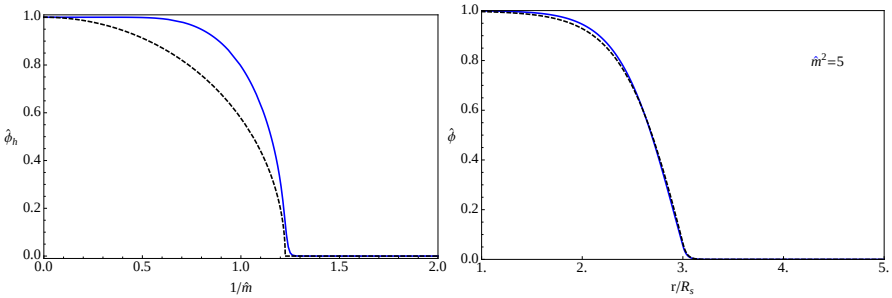


Figure 10: Comparing the analytics and numerics for the symmetron. On left the computed horizon value of the symmetron is shown in blue, together with the approximation in dashed black. On the right, the symmetron profile for $\hat{\mu} = \sqrt{5}$, $\hat{m} = 10\hat{\mu}$ is shown (in blue) compared to the analytic tanh profile (dashed black) approximation. Even though the mass is not particularly large, the approximation is extremely good.

accretion onto the black hole. Though it is possible that the fifth force effects could alter the structure of accretion disks [57], determining whether the effect could be observable would require astrophysical modelling beyond the scope of this paper. We can, however, study its effects on the dynamics of an orbiting test particle.

For a test particle at distance r from the black hole, the ratio of the fifth force to that of Newtonian gravity is

$$\frac{|F_\phi|}{|F_N|} \approx \left(\frac{r}{R_s}\right)^2 \beta(\phi)|\vec{\nabla}\phi|\frac{M_{BH}}{M_p^3}. \tag{4.1}$$

Our initial assumptions guarantee this to be small: In §3 we stated that a requirement for the Schwarzschild metric to be a good leading order background was $|T_\phi| \sim |\nabla\phi|^2 \ll \frac{M_p^6}{M_{BH}^2}$. For $\beta \sim \mathcal{O}(1)$, this condition is identical to requiring $|F_\phi/F_N| \ll 1$. For the profiles presented in §3, the largest fifth force will be generated by chameleons which vary rapidly in a thin shell near R_0. Inserting even the most optimistic parameter values shows that the ratio in (4.1) will be at most $\mathcal{O}(10^{-2})$. To evaluate the relevance of our estimated scalar gradients, we should study them in comparison to another small effect, namely gravitational radiation.

We can do this if we view our static black hole model as the supermassive partner of an extreme mass ratio inspiral (EMRI) binary system. Such EMRI systems, which consist of a stellar mass compact object orbiting a supermassive black hole, will be detectable by future space-based gravitational wave detectors [31]. In GR they will emit gravitational radiation at a rate approximated to leading order in $\dot{r}$ by, [58, 59],

$$\frac{dE}{dt} = -\left\langle \frac{m_t^2 G^3 M_{BH}^2}{c^5 r^4}\frac{8}{15}(12v^2 - 11\dot{r}^2)\right\rangle, \tag{4.2}$$

where m_t is the mass of in-falling object, v its velocity, r its radial position, and the angled brackets indicate an average over an orbital period. This emission will cause the orbiting object to gradually move to smaller radii, which we would detect as a decrease in the period of detected gravitational waves.

To leading, Newtonian, order, the gravitational binding energy of the system, per unit mass of the test particle, will be

$$\mathcal{E} = \frac{GM_{BH}}{r} - \frac{v^2}{2}. \tag{4.3}$$

The conservation of total energy allows us to relate the rate of change of this Newtonian energy to flux being carried away by gravitational waves $\dot{\mathcal{E}}_{GR}$ and interactions with scalar fifth forces $\dot{\mathcal{E}}_{\phi}$.

$$\dot{\mathcal{E}} = \dot{\mathcal{E}}_{GR} + \dot{\mathcal{E}}_{\phi}. \tag{4.4}$$

The evolving frequency of gravitational waves from a binary system tells us about rate of change of its orbital period, allowing us to measure $\dot{\mathcal{E}}$. Therefore, if the scalar fifth force can generate effects comparable to those of gravitational waves, it could potentially be detected by observations of EMRI systems.

A detailed examination of the chameleon, dilaton, and symmetron effects on EMRI signals would require a sophisticated treatment like that in [31], taking into account time-dependent effects on the scalar field as well as the fact that an accretion disk will affect EMRI dynamics even in GR [60, 61]. However, we find that if we model the stellar mass object as a test particle in orbit around the black hole, we are able to present an order-of-magnitude estimate for how the presence of a scalar fifth force will affect its gravitational binding energy.

The classical equation of motion for a test particle with mass m_t orbiting a black hole in the presence of a radial fifth force of magnitude $m_t a_\phi$ can be manipulated to show

$$\dot{\mathcal{E}}_{\phi} = v a_{\phi}. \tag{4.5}$$

Fifth force effects on in-falling particles are most likely to be important near $r = R_0$. Here we can estimate $|\dot{\mathbf{r}}|$ for an object in a bound orbit by equating centripetal acceleration with that of gravity, giving $v = \sqrt{\frac{GM}{R_0}} = \sqrt{\frac{R_S}{2R_0}}$. We note that at the innermost stable orbit $R_0 = 3R_S$, $v \sim \frac{1}{\sqrt{6}} \sim 0.4$. Such a large velocities signify a breakdown of Newtonian mechanics, however, since our goal is to derive an order of magnitude estimate of the effect, the approximation suffices.

We can now use our results from §3 to make a rough estimate for the scalar gradient, and thus, for the magnitude of the fifth force. When the scalar field mass in Region II is large, such as the case for the chameleon at accretion disc densities, we found that the field varies rapidly in a thin shell at the edge of the matter distribution. We can use our analytic approximation to estimate the scalar gradient near R_0 as

$$\left.\frac{d\phi}{dr}\right|_{R_0} \sim (\phi_* - \phi_h) \frac{m_*}{(m_* R_0)^{2/(n+2)}}\,. \tag{4.6}$$

For chameleons at galactic densities, and for dilatons, $m_\star R_0 \ll 1$, so the scalar will vary slowly everywhere. In this case we should instead write $\phi_{,r} \approx (\phi_\star - \phi_h)/R_0$.

Using these results we can estimate that when a test particle is near R_0, its rate of change in energy per unit mass due to the fifth force will be

$$\dot{\mathcal{E}}_{\phi} \approx \left(\sqrt{\frac{R_S}{2R_0}}\right) \frac{\beta}{M_p} \left(\frac{\phi_h - \phi_\star}{\Delta R}\right), \tag{4.7}$$

where ΔR is the smaller of R_0 or $R_0^{\frac{2}{n+2}} m_\star^{-\frac{n}{n+2}}$.

We note that for chameleons and dilatons $\phi_h > \phi_\star$, so $\dot{\mathcal{E}}_{\phi}$ will be positive. This is a reflection of the fact that the scalar force will manifest itself as an extra attraction between the test particle and the matter distribution $\rho(r)$. This can also be seen if we assume the test particle is a stellar mass black hole and write its scalar 'charge', in the sense of [55, 56, 62],

$Q(t) \propto \dot{\mathbf{r}}(t) \cdot \nabla\phi(\mathbf{r}(\mathbf{t}))$. We note that as the stellar mass black hole moves inwards through the scalar gradient, its 'charge' will increase, indicating that it will absorb energy from the scalar field. This suggests that the scalar profile generated by the interaction of screened modified gravity and an accretion disk or galactic halo will slow the inspiral of an EMRI system.

Comparing the scalar radiation to the gravitational wave effects gives

$$\left|\frac{\dot{\mathcal{E}}_\phi}{\dot{\mathcal{E}}_{GR}}\right| \sim \beta(\phi_\star)\left(\frac{R_0}{R_s}\right)^{\frac{9}{2}}\left(\frac{\phi_h-\phi_\star}{\Delta R}\right)\frac{M_{BH}}{M_p^3}\left[\frac{M_{BH}}{m_t}\right]. \tag{4.8}$$

The first part of this expression is the same (small) term that appeared in (4.1), indicating that the scalar fifth force will be small compared to that of Newtonian gravity. Because we are considering an EMRI system where $m_t \ll M_{BH}$, the final bracketed term will be large. Therefore, to be able to evaluate whether the scalar field induced energy evolution is comparable to that from quadrupole radiation in GR, we must insert physically relevant values for the various parameters.

Let us assume that the test mass is a solar mass black hole being captured by a super-massive black hole, which we will take to have a mass either $M_{BH} \sim 10^{6-9} M_\odot \sim 10^{44-47} M_p$. We can now use our results from §3 to estimate this relation for the scenarios where we predict a non-zero scalar gradient.

Short range chameleons

Chameleons are expected to have $m_\star R_0 \gg 1$ when the central black hole is surrounded by an accretion disk. For this case we set $\Delta R = R_0^{\frac{2}{n+2}} m_\star^{-\frac{n}{n+2}}$, and substituting for ϕ_h (eq. (3.25)) gives

$$\left|\frac{\dot{\mathcal{E}}_\phi}{\dot{\mathcal{E}}_{GR}}\right| \sim 10^{-28-60/(n+2)}\,\beta_*\frac{M_{BH}^2}{M_p m_t}\left(\frac{m_*}{M_p}\right)^{\frac{n}{n+2}} \tag{4.9}$$

where we have set $M \sim 10^{-3}\,\text{eV}$. If we assume that $\beta(\phi_\star) \sim \mathcal{O}(1)$ and reference Table 1 for chameleon masses, we find

$$\left|\frac{\dot{\mathcal{E}}_\phi}{\dot{\mathcal{E}}_{GR}}\right| \sim 10^{-23+\frac{2(n+3)}{(n+1)(n+2)}}\left(\frac{M_{BH}}{M_\odot}\right)^2 \approx 10^{-11} - 10^{-5} \tag{4.10}$$

for the super (or super-super) massive black holes, relatively independent of the index, n. Thus, chameleon fifth force effects on the test particle's dynamics will be much smaller than those of gravitational radiation. We note that because the non-zero fifth force operates only in a thin shell very near the ISCO, the effects will likely be more suppressed than this estimate suggests. However, should the chameleon model have a significant coupling parameter β, then these conclusions will be changed, as the ratio is proportional to β.

Long range chameleons

When the black hole is surrounded by matter with galactic halo density, it is possible that the chameleon will be light compared to the size of the system. For this case we use $\Delta R = R_0 \simeq 3R_S$ to get

$$\left|\frac{\dot{\mathcal{E}}_\phi}{\dot{\mathcal{E}}_{GR}}\right| \sim \beta\frac{(\phi_h-\phi_\star)}{M_p}\frac{M_{BH}}{m_t}. \tag{4.11}$$

The chameleon profile calculations in Section 3.1 then give

$$\left|\frac{\dot{\mathcal{E}}_\phi}{\dot{\mathcal{E}}_{GR}}\right| \sim 10^2\beta^2\,\frac{\rho_\star R_0^2}{2M_p^2}\frac{M_{BH}}{M_\odot} \sim 10^{-42}\beta^2\,\frac{\rho_\star}{\rho_{\rm cos}}\left(\frac{M_{BH}}{M_\odot}\right)^3 \sim 10^{-18} - 10^{-9} \tag{4.12}$$

where we assume $\beta \sim \mathcal{O}(1)$ and $\rho_* \sim 10^6\rho_{\rm cos}$. Once again, if the coupling function becomes appreciably large, this conclusion will change.

Dilatons

Dilatons will always always satisfy $m_\star R_0 \ll 1$, so we again use (4.11). From section 3.2, we find

$$\frac{\varphi_h - \varphi_\star}{M_p} \approx k(\phi_*)\delta\phi \sim \lambda\beta_*\frac{\rho_* R_0^2}{M_p^2} = \lambda\frac{\rho_{\rm cos}R_0^2}{M_p^2} \approx 10^{-42}\lambda\left(\frac{M_{BH}}{M_\odot}\right)^2 \tag{4.13}$$

using $\beta_* \simeq \rho_{\rm cos}/\rho_*$. We therefore find

$$\left|\frac{\dot{\mathcal{E}}_\phi}{\dot{\mathcal{E}}_{GR}}\right| \sim 10^{-42}\,\lambda\frac{\rho_{\rm cos}}{\rho_*}\left(\frac{M_{BH}}{M_\odot}\right)^3 \sim [10^{-24} - 10^{-15}]\lambda\left(\frac{\rho_{\rm cosm}}{\rho_\star}\right). \tag{4.14}$$

Clearly dilatons have a far weaker impact than chameleons on radiative loss.

5 Conclusions

The strong field, large curvature limit of modified gravity is a largely unexplored area for constraining various model dependent parameters and differentiating between the numerous models that exist in literature. By studying a static, spherically symmetric black hole with an r-dependent matter distribution around it, we were able to show that theories of modified gravity with screening mechanisms violate the no-hair theorems of GR and the scalar field can have a non-trivial profile. In this construction, we found that chameleon and dilaton fields develop a non-trivial scalar profile, while the symmetron assumes a constant value. An order of magnitude estimate of the effects of such a scalar gradient on in falling test particles was shown to generate effects that would be observationally challenging to detect and sub-leading compared to the quadruple radiation in GR.

Note that our findings for symmetrons could be qualitatively altered if we used a different matter distribution in our setup. As we discussed at the beginning of §3, if the matter density far from the black hole is small enough to make the symmetron approach $\phi_\star = \mu/\sqrt{\lambda}$ as its boundary condition, its field equation will no longer have a constant solution. This could occur, for example, if we used a model of an accretion disk which had finite spatial extent. We would, however, expect any symmetron gradients to be comparable to the ones found above for long range chameleons and dilatons.

Similar reasoning can be applied when we consider solutions to the scalar field equation with angular dependence, or solutions on a Kerr background. No hair theorems require that in a stationary system involving matter around a black hole, any gradient in the scalar field will be sourced entirely by non-uniformities in matter density. If we assume that the density contrasts examined above are typical of astrophysical matter distributions near black holes, the magnitude of the scalar gradients produced (and their consequent fifth forces) should likewise be representative. Thus generically we would expect theories of screened modified

gravity to produce solutions distinct from GR around stationary black hole systems with sub leading corrections to various observational effects.

It would be interesting to explore this strong field limit further. One possible physical effect to study within our setup would be the phase of gravitational waves. Our crude estimates suggest that the rate of GR quadruple radiation will dominate over any radiation in the scalar sector, however, in [63], the authors showed that in Brans-Dicke theory the presence of a massive scalar field affects the phasing of gravitational radiation from binary systems significantly and they found that for observations of intermediate mass ratio inspirals, this effect could be used to place constraints on model parameters (a lower bound on ω_{BD} and an upper bound on the mass of the scalar) which are competitive with Cassini and LLR measurements.

Additionally, the requirement that our system and solutions be stationary causes us to disregard the possibility of transient effects associated with superradiance. Superradiance is a property of rotating black holes through which incident waves with at resonant frequency can become amplified by extracting some of the black hole's rotational energy. A number of studies have shown that superradiant effects can give rise to long-lived unstable modes in the presence of a massive scalar [64–68]. This occurs for isolated black holes, but it also has been shown that when a black hole is surrounded by matter, superradiant modes can be amplified by factors as large as 10^5 [54]. If the scalar's mass is very light, the instability timescale for these modes becomes short and would result in gaps in the mass-spin phase space of observed black holes. Because of this, measurements of a black hole's mass and spin can be used to constrain allowed masses for scalar fields. This technique has already been used to place the most stringent upper bound on the mass of the photon [68, 69].

Yet another potentially observable effect of superradiance occurs in EMRI systems, in what is known as floating orbits [19, 31, 70]. Floating orbits occur when the orbital frequency of the small compact object can excite superradiant modes. This causes the scalar field to transfer rotational energy from the central black hole into the orbit of the small compact object, counteracting the energy lost through quadrupole radiation and slowing the inspiral. Such floating orbits would affect the EMRI's gravitational waveforms significantly, so the detection of an EMRI signal consistent with GR would allow us to place strong constraints on the mass of a light scalar.

We note with interest that these effects are typically studied in the context of scalar fields with a mass in the range $10^{-33}\,\mathrm{eV} - 10^{-10}\,\mathrm{eV}$ [69], which is relevant for dilatons and symmetrons, as well as chameleons at galactic or cosmological densities. Consideration of gravitational wave phasing, superradiant instabilities, and floating orbits will thus be important if we want to understand how these theories can be constrained by observations of black hole systems. We hope to further explore some of these effects in future works.

Acknowledgments

RG is supported in part by STFC (Consolidated Grant ST/J000426/1), in part by the Wolfson Foundation and Royal Society, and in part by Perimeter Institute for Theoretical Physics. Research at Perimeter Institute is supported by the Government of Canada through Industry Canada and by the Province of Ontario through the Ministry of Research and Innovation. RJ is supported by the Cambridge Commonwealth Trust and Trinity College, Cambridge. ACD is supported in part by STFC. JM was supported in Cambridge by a Marshall Scholarship.

This work was also supported in part by the National Science Foundation under Grant No. PHYS-1066293 and the hospitality of the Aspen Center for Physics.

References

[1] C. M. Will, "The Confrontation between general relativity and experiment," Living Rev. Rel. **9**, 3 (2006) [gr-qc/0510072].

[2] A. G. Riess *et al.* [Supernova Search Team Collaboration], "Observational evidence from supernovae for an accelerating universe and a cosmological constant," Astron. J. **116** (1998) 1009 [astro-ph/9805201].

[3] S. Perlmutter *et al.* [Supernova Cosmology Project Collaboration], "Measurements of Omega and Lambda from 42 high redshift supernovae," Astrophys. J. **517** (1999) 565 [astro-ph/9812133].

[4] G. Hinshaw *et al.* [WMAP Collaboration], "Nine-Year Wilkinson Microwave Anisotropy Probe (WMAP) Observations: Cosmological Parameter Results," Astrophys. J. Suppl. **208** (2013) 19 [arXiv:1212.5226 [astro-ph.CO]].

[5] P. A. R. Ade *et al.* [Planck Collaboration], "Planck 2013 results. XVI. Cosmological parameters," [arXiv:1303.5076 [astro-ph.CO]].

[6] K. N. Abazajian *et al.* [SDSS Collaboration], "The Seventh Data Release of the Sloan Digital Sky Survey," Astrophys. J. Suppl. **182** (2009) 543 [arXiv:0812.0649 [astro-ph]].

[7] T. Clifton, P. G. Ferreira, A. Padilla and C. Skordis, "Modified Gravity and Cosmology," Phys. Rept. **513** (2012) 1 [arXiv:1106.2476 [astro-ph.CO]].

[8] B. Bertotti, L. Iess, and P. Tortora, "A test of general relativity using radio links with the Cassini spacecraft," *Nature* **425** (Sept., 2003).

[9] J. G. Williams, S. G. Turyshev and D. H. Boggs, "Progress in lunar laser ranging tests of relativistic gravity," Phys. Rev. Lett. **93** (2004) 261101 [gr-qc/0411113].

[10] J. Khoury and A. Weltman, "Chameleon cosmology," Phys. Rev. D **69** (2004) 044026 [astro-ph/0309411].

[11] P. Brax, C. van de Bruck, A. -C. Davis and D. Shaw, "The Dilaton and Modified Gravity," Phys. Rev. D **82** (2010) 063519 [arXiv:1005.3735 [astro-ph.CO]].

[12] K. Hinterbichler, J. Khoury, A. Levy and A. Matas, "Symmetron Cosmology," Phys. Rev. D **84** (2011) 103521 [arXiv:1107.2112 [astro-ph.CO]].

[13] D. F. Mota and D. J. Shaw, "Beyond the Chameleon Mechanism," [arXiv:0805.3430 [hep-ph]].

[14] A. Upadhye, "Symmetron dark energy in laboratory experiments," Phys. Rev. Lett. **110** (2013) 031301, [arXiv:1210.7804 [hep-ph]].

[15] A. Upadhye, "Dark energy fifth forces in torsion pendulum experiments," Phys. Rev. D **86** (2012) 102003 [arXiv:1209.0211 [hep-ph]].

[16] A. Upadhye, "Particles and forces from chameleon dark energy," [arXiv:1211.7066 [hep-ph]].

[17] B. Jain and J. Khoury, "Cosmological Tests of Gravity," Annals Phys. **325** (2010) 1479 [arXiv:1004.3294 [astro-ph.CO]].

[18] B. Jain, V. Vikram and J. Sakstein, "Astrophysical Tests of Modified Gravity: Constraints from Distance Indicators in the Nearby Universe," Astrophys. J. **779** (2013) 39 [arXiv:1204.6044 [astro-ph.CO]].

[19] N. Yunes and X. Siemens, "Gravitational Wave Tests of General Relativity with Ground-Based Detectors and Pulsar Timing Arrays," Living Rev. Rel. **16** (2013) 9 [arXiv:1304.3473 [gr-qc]].

[20] D. Psaltis, "Probes and Tests of Strong-Field Gravity with Observations in the Electromagnetic Spectrum," *Living Rev. Relativity* **11** (2008).

[21] R. Ruffini and J. Wheeler, "Introducing the black hole," *Physics Today* **24** (1971) 30–36.

[22] A. Achucarro, R. Gregory and K. Kuijken, "Abelian Higgs hair for black holes," Phys. Rev. D **52**, 5729 (1995) [gr-qc/9505039].

[23] R. Bartnik and J. Mckinnon, "Particle - Like Solutions of the Einstein Yang-Mills Equations," Phys. Rev. Lett. **61**, 141 (1988).

[24] K. -M. Lee, V. P. Nair and E. J. Weinberg, "Black holes in magnetic monopoles," Phys. Rev. D **45**, 2751 (1992) [hep-th/9112008].

[25] S. R. Coleman, J. Preskill and F. Wilczek, "Growing hair on black holes," Phys. Rev. Lett. **67**, 1975 (1991).

[26] F. Dowker, R. Gregory and J. H. Traschen, "Euclidean black hole vortices," Phys. Rev. D **45**, 2762 (1992) [hep-th/9112065].

[27] J. D. Bekenstein, "Black hole hair: 25 - years after," In *Moscow 1996, 2nd International A.D. Sakharov Conference on physics* 216-219 [gr-qc/9605059].

[28] T. P. Sotiriou and V. Faraoni, "Black holes in scalar-tensor gravity," Phys. Rev. Lett. **108** (2012) 081103 [arXiv:1109.6324 [gr-qc]].

[29] V. Faraoni and T. P. Sotiriou, Absence of scalar hair in scalar-tensor gravity," [arXiv:1303.0746 [gr-qc]].

[30] T. P. Sotiriou and S. -Y. Zhou, "Black hole hair in generalized scalar-tensor gravity," arXiv:1312.3622 [gr-qc].

[31] N. Yunes, P. Pani and V. Cardoso, "Gravitational Waves from Quasicircular Extreme Mass-Ratio Inspirals as Probes of Scalar-Tensor Theories," Phys. Rev. D **85** (2012) 102003 [arXiv:1112.3351 [gr-qc]].

[32] S. Mirshekari and C. M. Will, "Compact binary systems in scalar-tensor gravity: Equations of motion to 2.5 post-Newtonian order," Phys. Rev. D **87** (2013) 8, 084070 [arXiv:1301.4680 [gr-qc]].

[33] J. Healy, T. Bode, R. Haas, E. Pazos, P. Laguna, D. M. Shoemaker, and N. Yunes, "Late Inspiral and Merger of Binary Black Holes in Scalar-Tensor Theories of Gravity," [arXiv:1112.3928].

[34] S. Chadburn and R. Gregory, *Time dependent black holes and scalar hair*, [arXiv:1304.6287 [gr-qc]].

[35] O. A. Fonarev, "Exact Einstein scalar field solutions for formation of black holes in a cosmological setting," Class. Quant. Grav. **12**, 1739 (1995) [gr-qc/9409020].

[36] T. Clifton, D. F. Mota and J. D. Barrow, "Inhomogeneous gravity," Mon. Not. Roy. Astron. Soc. **358**, 601 (2005) [gr-qc/0406001].

[37] T. Clifton, "Spherically Symmetric Solutions to Fourth-Order Theories of Gravity," Class. Quant. Grav. **23**, 7445 (2006) [gr-qc/0607096].

[38] G. C. McVittie, "The mass-particle in an expanding universe," Mon. Not. Roy. Astron. Soc. **93**, 325 (1933).

[39] J. Sultana and C. C. Dyer, "Cosmological black holes: A black hole in the Einstein-de Sitter universe," Gen. Rel. Grav. **37**, 1347 (2005).

[40] V. Faraoni and A. Jacques, "Cosmological expansion and local physics," Phys. Rev. D **76**, 063510 (2007) [arXiv:0707.1350 [gr-qc]].

[41] M. Carrera and D. Giulini, "On the influence of global cosmological expansion on the dynamics and kinematics of local systems," Rev. Mod. Phys. **82** 169 (2010 [arXiv:0810.2712 [gr-qc]].

[42] D. C. Guariento, M. Fontanini, A. M. da Silva and E. Abdalla, "Realistic fluids as source for dynamically accreting black holes in a cosmological background," Phys. Rev. D **86**, 124020 (2012) [arXiv:1207.1086 [gr-qc]].

[43] E. Abdalla, N. Afshordi, M. Fontanini, D. C. Guariento and E. Papantonopoulos, "Cosmological black holes from self-gravitating fields," [arXiv:1312.3682 [gr-qc].

[44] P. Brax, A. -C. Davis, B. Li, H. A. Winther and G. -B. Zhao, "Systematic simulations of modified gravity: chameleon models," JCAP **1304** (2013) 029 [arXiv:1303.0007 [astro-ph.CO]].

[45] P. Brax, "Lectures on Screened Modified Gravity," [arXiv:1211.5237 [hep-th]].

[46] D. F. Mota and D. J. Shaw, "Evading Equivalence Principle Violations, Cosmological and other Experimental Constraints in Scalar Field Theories with a Strong Coupling to Matter," Phys. Rev. D **75** (2007) 063501 [hep-ph/0608078].

[47] P. Brax, C. van de Bruck, A. -C. Davis, J. Khoury and A. Weltman, "Detecting dark energy in orbit - The Cosmological chameleon," Phys. Rev. D **70** (2004) 123518 [astro-ph/0408415].

[48] T. Damour and A. M. Polyakov, "The String dilaton and a least coupling principle," Nucl. Phys. B **423** (1994) 532 [hep-th/9401069].

[49] D. J. Kapner, T. S. Cook, E. G. Adelberger, J. H. Gundlach, B. R. Heckel, C. D. Hoyle and H. E. Swanson, "Tests of the gravitational inverse-square law below the dark-energy length scale," Phys. Rev. Lett. **98** (2007) 021101 [hep-ph/0611184].

[50] P. Brax, A. -C. Davis, B. Li and H. A. Winther, "A Unified Description of Screened Modified Gravity," Phys. Rev. D **86** (2012) 044015 [arXiv:1203.4812 [astro-ph.CO]].

[51] P. Brax, A. -C. Davis, B. Li, H. A. Winther and G. -B. Zhao, "Systematic Simulations of Modified Gravity: Symmetron and Dilaton Models," JCAP **1210** (2012) 002 [arXiv:1206.3568 [astro-ph.CO]].

[52] J. Clampitt, B. Jain and J. Khoury, "Halo Scale Predictions of Symmetron Modified Gravity," JCAP **1201** (2012) 030 [arXiv:1110.2177 [astro-ph.CO]].

[53] J. Khoury, "Theories of Dark Energy with Screening Mechanisms," [arXiv:1011.5909 [astro-ph.CO]].

[54] V. Cardoso, I. P. Carucci, P. Pani and T. P. Sotiriou, "Matter around Kerr black holes in scalar-tensor theories: scalarization and superradiant instability," Phys. Rev. D **88** (2013) 044056 [arXiv:1305.6936 [gr-qc]].

[55] M. W. Horbatsch and C. P. Burgess, "Cosmic Black-Hole Hair Growth and Quasar OJ287," JCAP **1205** (2012) 010 [arXiv:1111.4009 [gr-qc]].

[56] E. Berti, V. Cardoso, L. Gualtieri, M. Horbatsch and U. Sperhake, "Numerical simulations of single and binary black holes in scalar-tensor theories: circumventing the no-hair theorem," Phys. Rev. D **87** (2013) 124020 [arXiv:1304.2836 [gr-qc]].

[57] D. Perez, G. E. Romero and S. E. P. Bergliaffa, "Accretion disks around black holes in modified strong gravity," Astronomy & Astrophysics **551** (2013) arXiv:1212.2640 [astro-ph.CO].

[58] C. Will, *Theory and experiment in gravitational physics*, Cambridge University Press, 1993.

[59] P. Peters and J. Mathews, "Gravitational Radiation from Point Masses in a Keplerian Orbit," *Physical Review* **131** (July, 1963).

[60] B. Kocsis, N. Yunes, and A. Loeb, "Observable Signatures of EMRI Black Hole Binaries Embedded in Thin Accretion Disks," Phys. Rev. D **84** (2011) 024032 [arXiv:1104.2322 [astro-ph.GA]].

[61] N. Yunes, B. Kocsis, A. Loeb and Z. Haiman, "Imprint of Accretion Disk-Induced Migration on Gravitational Waves from Extreme Mass Ratio Inspirals," Phys. Rev. Lett. **107** (2011) 171103 [arXiv:1103.4609 [astro-ph.CO]].

[62] T. Jacobson, "Primordial black hole evolution in tensor scalar cosmology," Phys. Rev. Lett. **83** (1999) 2699 [astro-ph/9905303].

[63] E. Berti, L. Gualtieri, M. Horbatsch and J. Alsing, "Light scalar field constraints from gravitational-wave observations of compact binaries," Phys. Rev. D **85** (2012) 122005 [arXiv:1204.4340 [gr-qc]].

[64] V. Cardoso and S. Yoshida, "Superradiant instabilities of rotating black branes and strings," JHEP **0507** (2005) 009 [hep-th/0502206].

[65] S. R. Dolan, "Instability of the massive Klein-Gordon field on the Kerr spacetime," Phys. Rev. D **76** (2007) 084001 [[arXiv:0705.2880 [gr-qc]]].

[66] S. R. Dolan, "Superradiant instabilities of rotating black holes in the time domain," Phys. Rev. D **87** (2013) 124026, [arXiv:1212.1477 [gr-qc]].

[67] H. Witek, V. Cardoso, A. Ishibashi and U. Sperhake, "Superradiant instabilities in astrophysical systems," Phys. Rev. D **87** (2013) 043513 [arXiv:1212.0551 [gr-qc]].

[68] V. Cardoso, "Black hole bombs and explosions: from astrophysics to particle physics," Gen. Rel. Grav. **45** (2013) 2079, [arXiv:1307.0038 [gr-qc]].

[69] E. Berti, "Astrophysical black holes as natural laboratories for fundamental physics and strong-field gravity," Braz. J. Phys. **43** (2013) 341, [arXiv:1302.5702 [gr-qc]].

[70] V. Cardoso, S. Chakrabarti, P. Pani, E. Berti and L. Gualtieri, "Floating and sinking: The Imprint of massive scalars around rotating black holes," Phys. Rev. Lett. **107** (2011) 241101 [arXiv:1109.6021 [gr-qc]].